



The late Pleistocene Sacarosa tephra-fall deposit, Misti Volcano, Arequipa, Peru: its magma, eruption, and implications for past and future activity

Christopher J. Harpel¹ · Juan José Cuno^{2,3} · Marie K. Takach^{4,5} · Marco Rivera⁶ · Rigoberto Aguilar³ · Frank J. Tepley III⁴ · Fredy Garcia²

Received: 12 October 2022 / Accepted: 26 May 2023 / Published online: 14 August 2023

This is a U.S. Government work and not under copyright protection in the US; foreign copyright protection may apply 2023

Abstract

Between 38.5 ka cal BP and 32.4 ka cal BP, a dacitic Volcanic Explosivity Index 5 eruption at Misti volcano emplaced the Sacarosa tephra-fall deposit. Its biotite phenocrysts, fine grain size, scarce lithics, and abundant loose crystals characterize the deposit at locations sampled. The eruption's ~800 °C magma rose rapidly from ~10 km depth, culminating in a Plinian eruption which reached a mass eruption rate of 7.7×10^6 – 4.1×10^7 kg/s and emplaced about 3 km³ of tephra within tens of hours. The unit comprises two layers of subequal thickness separated by a diffuse contact with the upper distinguished by being slightly coarser and less well sorted than the lower. The deposit's coarser upper layer indicates either climactic conditions or a lesser degree of fragmentation during the latter half of the eruption. Strong winds distributed the deposit southwest of Misti, where it crops out over at least 800 km² and drapes the present site of Arequipa with up to 100 cm of tephra. The Sacarosa deposit is the first among the Cayma stage deposits, a distinctive group of felsic, biotite-bearing units, to be carefully described and its eruption characterized. Several Cayma stage deposits were emplaced by voluminous explosive eruptions similar to the Sacarosa eruption, representing a ~8.9–15.5 ky interval of powerful eruptions. Such an explosive eruption today would threaten Arequipa's over 1,100,000 residents, many of whom live within the Sacarosa deposit's distribution.

Keywords Misti volcano · Cayma stage · Plinian eruption · Tephrostratigraphy · Magma conditions · Dacite

Resumen Entre 38.5 ka cal BP y 32.4 ka cal BP el volcán Misti generó una erupción dacítica con Índice de Explosividad Volcánica 5 que emplazó el depósito de caída de tefra “Sacarosa”. La presencia de fenocristales de biotita, el tamaño fino de sus granos, escasos líticos y la abundancia de cristales libres caracterizan el depósito en los lugares muestreados. El magma tuvo una temperatura de ~800 °C, el cual ascendió rápidamente de ~10 km de profundidad y resultó en una erupción Pliniana que tuvo una tasa de descarga de masa de 7.7×10^6 – 4.1×10^7 kg/s, y depósito alrededor de 3 km³ de tefra dentro de decenas de horas. El depósito tiene dos capas con espesores casi similares, separados por un contacto difuso y con una capa superior que se caracteriza por contener granos un poco más gruesos y ser un poco menos sorteado que la capa inferior. La capa superior gruesa indica condiciones culminantes o un menor grado de fragmentación durante la última mitad de la erupción. Fuertes vientos distribuyeron el depósito al suroeste del Misti cubriendo al menos 800 km², incluyendo la actual ciudad de Arequipa donde el depósito de tefra tiene hasta 100 cm de espesor. El depósito “Sacarosa” es el primero entre los depósitos de

Editorial responsibility: N. Pardo

✉ Christopher J. Harpel
charpel@usgs.gov

¹ U.S. Geological Survey, Volcano Disaster Assistance Program, Cascades Volcano Observatory, Vancouver, WA, USA

² Escuela Profesional de Ingeniería Geológica, Universidad Nacional de San Agustín, Arequipa, Peru

³ Instituto Geológico, Minero Y Metalúrgico del Perú, Observatorio Vulcanológico del INGEMMET, Yanahuara, Arequipa, Peru

⁴ College of Earth, Ocean, and Atmospheric Sciences, Oregon State University, Corvallis, OR, USA

⁵ Present Address: Department of Geological Sciences, Central Washington University, Ellensburg, WA, USA

⁶ Instituto Geofísico del Perú, Observatorio Vulcanológico del Sur, Sachaca, Arequipa, Peru

la etapa Cayma (un grupo distintivo de unidades félsicas que contienen biotita) que es descrito detalladamente y con su erupción caracterizada. Varios depósitos de la etapa Cayma fueron generados por erupciones explosivas voluminosas similares a la erupción “Sacarosa”, representando un intervalo de ~8.9–15.5 ky de poderosas erupciones. Una erupción tan explosiva hoy amenazaría a los más de 1,100,000 habitantes de Arequipa, muchos de ellos viven dentro del área de distribución del depósito “Sacarosa”.

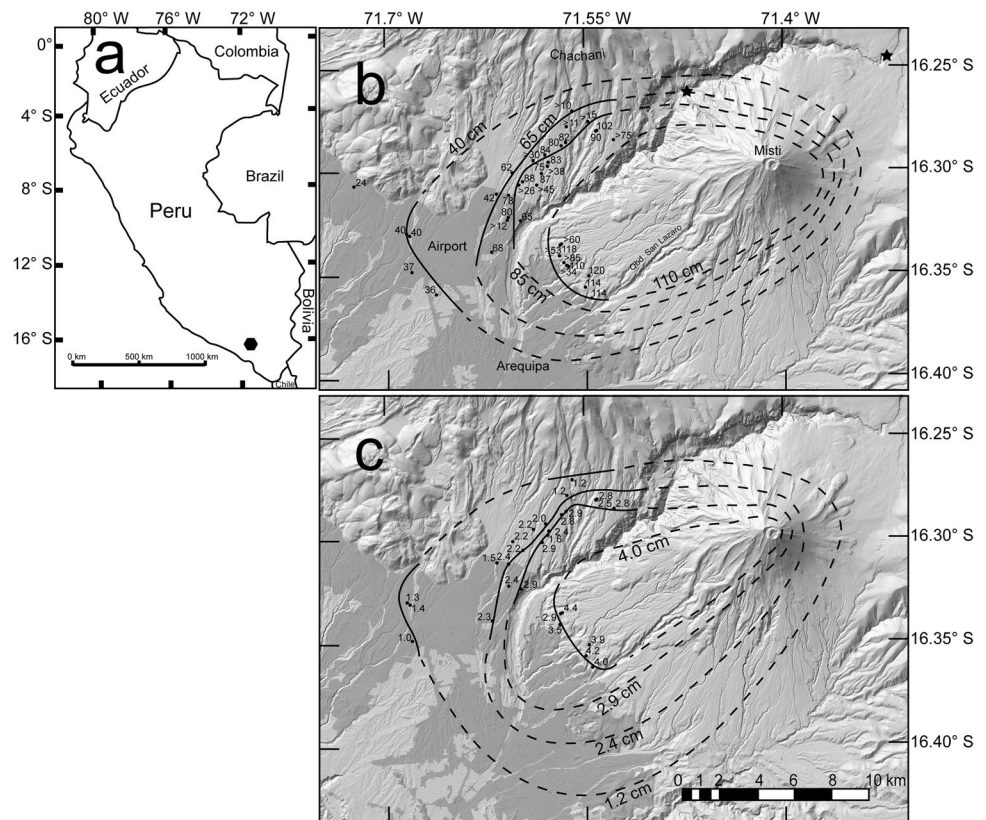
Introduction

Misti volcano has a history of explosive eruptions that emplaced numerous tephra-fall deposits (TFDs; Legros 2001; Mariño et al. 2016; Harpel et al. 2021). The city of Arequipa (Fig. 1), built upon many of these deposits, has a growing population of over 1,100,000 (Instituto Nacional de Estadística e Informática 2018) and critical infrastructure in high volcanic hazard zones (Mariño et al. 2007). Arequipa is nestled among the massive Plio-Pleistocene Pichu Pichu (Guevara 1968; Bernahola Portugal 2018) and Pleistocene Chachani (Aguilar et al. 2022) volcanic complexes, and Misti, a voluminous, youthful cone with documented Holocene eruptions (Thouret et al. 2001). Misti is currently fumarolic (Birnie and Hall 1974; Moussallam et al. 2017; Vlastelic et al. 2022) and has experienced historical periods of

unrest and enhanced degassing, some of which were possibly accompanied by small-volume phreatic or phreatomagmatic eruptions and the most recent of which occurred in 1985 (Hantke and Parodi 1966; Masías Nuñez del Prado 1997). A mid-fifteenth century eruption, which built the summit cinder cone and distributed ash locally, was incorporated into the indigenous population’s oral history and possibly provoked human sacrifices (Chávez Chávez 1992; Socha et al. 2021). Misti’s most recent Plinian eruption occurred ~2 ka, emplacing voluminous deposits, which now underly parts of Arequipa (Harpel et al. 2011; Cobeñas et al. 2012). Thouret et al. (2001) broadly delineated Misti’s history. Yet to date, only the Autopista, Sandwich Inferior, Sandwich Superior, and 2-ka deposits have been individually investigated (e.g., Cacya et al. 2007; Harpel et al. 2011; Escobar 2021), leaving deposits from most of Misti’s eruptions uncharacterized and their hazards implications unknown.

Within the Andean Central Volcanic Zone (CVZ), five Holocene or historical eruptions with Volcanic Explosivity Index (VEI; Newhall and Self 1982) 5 or greater are documented (Siebert et al. 2010) with only Misti’s ~2-ka (VEI 5), Huaynaputina’s 1600-CE (VEI 6), and Cerro Blanco’s 4.2-ka-cal-BP (VEI 7) eruptions exhaustively volcanologically characterized (e.g., Adams et al. 2001; Harpel et al. 2011; Fernandez-Turiel et al. 2019). Huaynaputina’s paroxysm remains the most powerful historical Andean eruption, which in addition to catastrophic economic and social

Fig. 1 **a** Map of Peru with Arequipa and Misti indicated by the black hexagon. **b** Isopach map for the Sacarosa tephra-fall deposit. Thickness in centimeters is indicated at each point. The locations of Arequipa, the airport, Misti, Chachani, and Quebrada San Lazaro are indicated. Black stars indicate the Aguada Blanca hydroelectric installation. **c** Pumice isopleth map. Average maximum pumice size in centimeters is at each point. Dark gray shading in **a** and **c** represents Arequipa’s urbanized area. Isopachs and isopleths indicated with solid lines are constrained by field data and dashed lines are inferred



consequences for Peru, caused global impacts such as unseasonably cold weather, crop failures, and epidemics in Asia during 1601 CE (e.g., de Silva et al. 2000; Fei et al. 2016; Mariño et al. 2021). Whereas such events are rare, occurring once a decade or more worldwide (Siebert et al. 2010), they are commonly under-represented in eruption catalogs (Kiyosugi et al. 2015). Recent work at other volcanoes in the Peruvian CVZ, such as Ubinas (Wright et al. 2018; Samaniego et al. 2020), Sara Sara (Cueva 2016; Rivera et al. 2020a), and Yucamane-Calientes (Rivera et al. 2020b) suggests that more VEI 5 or greater eruptions probably have occurred but remain to be characterized in detail.

A distinct group of at least three biotite-bearing dacite and rhyolite deposits emplaced sometime between about 50 ka and 20 ka punctuates Misti's history, which is dominated by pyroxene- and amphibole-bearing andesites (e.g., Legros 1998; Thouret et al. 2001; Mariño et al. 2016). Available data from these felsic deposits, emplaced during an eruptive period which we informally name the Cayma stage, imply that they are products of powerful explosive eruptions (e.g., Legros 1998; Mariño et al. 2016; Cuno 2018). The Sacarosa TFD was emplaced by one of these eruptions sometime between 33.7 ka and 20 ka (Legros 2001; Mariño et al. 2016; Cuno 2018).

Characterizing the magmatic conditions leading to the Sacarosa eruption is the first step in understanding the origin and evolution of the broader Cayma stage eruptions (Topham et al. 2021), which is key to understanding if future similarly powerful explosive silicic events could occur. Additionally, multiple subsequent eruptions, including Misti's most recent Plinian event at 2 ka, produced mingled pumice of dominant andesite and minor felsic components (Tepley et al. 2013; Takach et al. 2021, in review). Such felsic components in products from recent eruptions highlight the continued impact of silicic magmas on Misti's eruptive behavior and importance in understanding them.

Future powerful explosive eruptions would severely disrupt Arequipa. By characterizing the Sacarosa TFD, its distribution, and its eruption's dynamics, we provide the first comprehensive description of one of Misti's Cayma stage eruptions and its implications for future hazards. We further determine the Sacarosa magma's pre-eruption conditions and provide the first insights into Misti's late Pleistocene silicic magmatic system.

Methods

We document the Sacarosa TFD at 40 sites with deposit thickness recorded at 36 of these locations. At 28 sites, the five largest pumice were measured and averaged. Data were collected from sites on flat or gently sloping surfaces and where the deposit was not obviously over-thickened by dry

ravel. At locations where post-emplacment erosion of the deposit is evident, thicknesses are considered minima. The scarcity of lithics precluded their measurement. Samples from eight sites, including sub-samples from the deposit's layers, were hand sieved to determine their grain-size distribution. Componentry was determined for bulk samples by point-counting 1000–1756 clasts per sample for the 125–500 μm fractions. For grain sizes greater than 2–4 mm, components were segregated, weighed, and their masses converted to volume percentages using average clast densities. Density was measured on 89 pumice from six bulk tephra samples.

Whole-rock geochemical analysis includes X-ray fluorescence on nine samples at the Washington State University GeoAnalytical Laboratory (WSU) and Hamilton Analytical Laboratory (HAL) following the methods of Johnson et al. (1999). Trace-element concentrations were measured for one sample at WSU using inductively coupled plasma-mass spectrometry (ICP-MS) and three samples at HAL using laser-ablation ICP-MS following the methods of Conrey et al. (2023).

The Sacarosa pumice were petrographically characterized in six thin sections and their glass and phenocryst compositions subsequently determined at Oregon State University using a CAMECA SX-100 electron microprobe with five wavelength-dispersive spectrometers and high-intensity dispersive crystals for high-sensitivity analysis. Glass and minerals were analyzed using a 15 keV accelerating voltage and 10 and 30 nA sample currents, respectively. Beam sizes were 1 μm for Fe-Ti oxides, 5 μm for plagioclase, amphibole, and biotite, and 10 μm for glass. Count times ranged from 10 to 120 s depending on the element and desired detection limit. Alkali migration was mitigated by applying zero-time intercept functions. Typical one standard deviation precision for each phase is listed in Table 1. Back-scattered electron images were obtained on this instrument using the CAMECA PeakSight software.

Charcoal and organic material were collected for ^{14}C dating at three sites within 10 cm of the Sacarosa TFD's basal contact. At one of the sites, two additional samples of organic material were collected from a layer of reworked sediment ~3–4 m above the Sacarosa deposit. The samples were dated by Beta Analytic Inc., PaleoResearch Institute, and the U.S. Geological Survey Radiocarbon Laboratory in Reston, VA, using the accelerator mass spectrometry method. Ages were calibrated in OxCal 4.4.4 (Bronk Ramsey 2009; Bronk Ramsey and Lee 2013) using a mixed calibration curve model allowing for any proportion of the IntCal20 (Reimer et al. 2020) and SHCal20 (Hogg et al. 2020) curves to impact the modeled ages (Ogburn 2012; Marsh et al. 2018). Published ages were calibrated using the same method. For a detailed discussion of our ^{14}C age calibration and mixed curve model, see Electronic Supplementary Material (ESM) 1.

Cayma stage stratigraphic context

The Sacarosa TFD is one of the voluminous Cayma stage deposits given a variety of names by previous workers. Legros (1998, 2001) characterized and designated the units from lowest to highest as R1, R2, D1, and D2, with the R2 TFD intercalated between coeval pyroclastic-density-current (PDC) deposits, including the underlying R1 PDC deposit (Fig. 2). Mariño et al. (2016) provided additional descriptions and informally designated the same TFDs Fibroso I (R2), Sacaroso (D1), and Fibroso II (D2). The TFD dated by Ayala-Arenas et al. (2019) is ostensibly correlated to Mariño et al.'s (2016) Fibroso I unit. Cacya et al. (2007) and Cuno (2018) subsequently applied the names Sacaroide and Sacarosa to the Sacaroso, respectively.

We follow Cuno (2018) and informally apply the name Sacarosa to the unit variously referred to as D1, Sacaroide, and Sacaroso (Legros 2001; Cacya et al. 2007; Mariño et al. 2016). The similarity of the Fibroso I and Fibroso II names on unrelated units causes confusion. So, we informally rename the TFDs Cogollo and Conchito, respectively (Fig. 2). We also informally name and describe for the first time the Anchi TFD, which crops out between the Cogollo and Sacarosa TFDs (ESM 2).

Southwest of Misti, our observations generally support Legros' (2001) stratigraphy, but south and east of Misti, the Sacarosa TFD is locally overlain by perhaps two or more Cayma stage TFDs. At one location, the outcrop is complex (Fig. 2c), not fully characterized, and faulting may have caused repeated sequences of TFDs. Several units at the site, nonetheless, appear primary and in stratigraphic order despite such faulting and minor erosional unconformities. We informally name the uppermost Cayma stage unit at the site the Chuma TFD and provide a preliminary description of it in ESM 2. The Sacarosa TFD is the third from the base of the Cayma stage. Legros (2001) also observed additional Cayma stage deposits southeast of Misti (Fig. 2c), which may correlate to units between the Sacarosa and Chuma deposits. ESM 2 provides additional discussion of the Cayma stage stratigraphy and some of its important units.

Deposit characteristics

The Sacarosa TFD is white but locally weathered to pale yellow, commonly crops out at or within several meters of the modern surface, and mantles paleo-topography beneath it. As Legros (2001) noted, it commonly overlies a dark brown paleosol, which frequently contains charcoal. This paleosol is sufficiently pervasive and distinct among the poorly developed paleosols and organic-poor sandy and silty layers of reworked sediment that more commonly

underly Misti's deposits that it facilitates identification of the Sacarosa TFD. The unit consists of two massive layers, about equally thick, separated by a diffuse contact, and differentiated by the upper layer's slightly coarser grain size and poorer sorting (Fig. 3; ESM 3). The unit and both of its layers are well sorted (per Cas and Wright 1987). With mean grain sizes (Md_{ϕ}) from 1.9–0.6 mm (ESM 3), the Sacarosa TFD is commonly finer-grained than other TFDs of similar thickness at the same outcrop. Within the area investigated, the deposit's 125–500 μm fraction also consists mostly of loose crystals (ESM 4). Sacarosa pumice are subangular to subrounded (Fig. 3b, c). Lithics are aphanitic and porphyritic, dominantly red or orange with a minor proportion of gray clasts (Fig. 3d), and conspicuously sparse, composing ≤ 0.2 vol.% of the deposit (ESM 5) at proximal sites. We do not observe lithic-rich layers, despite Mariño et al. (2016) reporting such concentrations at the unit's base and middle.

Petrology and geochemistry

We differentiate two types of Sacarosa pumice based on their textural characteristics (Table 2). Type 1 pumice are volumetrically dominant, have an average density of ~ 500 kg/m^3 (ESM 6; Harpel et al. 2023), larger crystals, bimodal vesicle sizes, and are white. Some type 1 pumice have small, uncommon domains of deformed glass and bubbles. Type 2 pumice are light gray, fine grained, microvesicular, have slightly oxidized glass and phenocrysts, and an average density of ~ 800 kg/m^3 (ESM 6; Harpel et al. 2023). Rare pumice with mingled type 1 and 2 textures are also present, composing ≤ 4 vol.% of the deposit that is > 2 mm (ESM 6). The proportions of the two pumice types are the same in the deposit's upper and lower layers. Glass compositions are predominantly rhyolitic from 69 to 75 wt.% SiO_2 , while 10% of analyses are within an andesitic-dacitic compositional range of 62 to 66 wt.% SiO_2 (Table 1). The latter glass compositions are primarily related to type 2 pumice. Glass in both pumice types lacks microlites. Phenocrysts of plagioclase, amphibole, biotite, and Fe-Ti oxides are present in both pumice types, though type 2 contains only trace amounts of biotite. Quartz is not present in our samples, contrary to Mariño et al.'s (2016) observation.

The Sacarosa pumice have dacitic whole-rock compositions (Table 3; Harpel et al. 2023) with type 1 slightly more silicic (65.0–65.6 wt.% SiO_2 ; normalized to an anhydrous basis) than type 2 (64.0–64.2 wt.% SiO_2). Legros' (1998) D1 whole-rock data coincide with our Sacarosa data, thus supporting our correlation (Figs. 2 and 4a). The deposit's trace-element concentrations (Fig. 4b) have variable enrichment in

Table 1 Representative compositions of glass, plagioclase, amphibole, biotite, and Fe-Ti oxides

Glass										
Sample	MI16-01	MI16-01	MI16-01	MIS-17-17M	MIS-17-17M	MIS-17-18F	MIS-17-18F	MIS-17-18F	MIS-17-41C	MIS-17-41C
SiO ₂	71.65	74.14	63.95	72.97	71.43	71.93	71.67	65.04	72.92	74.45
TiO ₂	0.17	0.18	0.52	0.15	0.17	0.16	0.15	0.43	0.14	0.17
Al ₂ O ₃	12.77	12.61	14.93	12.63	12.76	12.74	12.67	15.26	12.60	12.57
FeO ^{Total}	0.93	1.00	3.23	0.93	1.00	1.13	1.01	3.11	1.03	0.96
MnO	0.07	0.06	0.09	0.04	0.11	0.06	0.06	0.06	0.04	0.04
MgO	0.24	0.23	2.50	0.23	0.26	0.27	0.25	1.42	0.27	0.26
CaO	1.20	1.18	3.63	1.29	1.21	1.16	1.29	4.33	1.22	1.14
Na ₂ O	3.93	3.24	3.86	2.77	4.06	3.44	3.75	4.38	3.40	3.75
K ₂ O	3.30	3.32	2.93	3.25	3.37	3.49	3.65	2.94	3.31	3.55
P ₂ O ₅	0.02	0.03	0.15	0.06	0.02	0.06	0.03	0.07	0.02	0.00
Cl	0.13	0.15	0.10	0.14	0.14	0.13	0.11	0.09	0.14	0.13
Total	94.43	96.14	95.96	94.49	94.56	94.57	94.65	95.98	95.11	97.05
Plagioclase										
Sample	MI16-01	MI16-01	MI16-01	MIS-17-18F	MIS-17-18F	MIS-17-18F	MIS-17-41C	MIS-17-41C	MIS-17-41C	MIS-17-41C
Crystal	plag 5	plag 5	plag 5	plag 2	plag 2	plag 2	plag 5	plag 5	plag 5	plag 5
Location	core	mid	rim	core	mid	rim	core	mid	rim	rim
SiO ₂	58.96	55.94	53.46	54.55	59.65	58.19	55.99	54.34	58.12	58.12
Al ₂ O ₃	26.00	27.63	28.34	29.02	25.68	26.50	27.96	29.33	26.19	26.19
FeO ^{Total}	0.18	0.21	0.38	0.21	0.20	0.24	0.18	0.24	0.21	0.21
MgO	0.00	0.01	0.03	0.01	0.01	0.01	0.01	0.01	0.00	0.00
CaO	7.95	9.70	12.05	10.77	7.42	8.35	9.99	11.34	8.00	8.00
Na ₂ O	6.36	5.58	4.41	4.86	6.70	6.11	5.45	4.57	6.17	6.17
K ₂ O	0.38	0.28	0.21	0.22	0.40	0.34	0.25	0.18	0.37	0.37
TiO ₂	0.01	0.01	0.01	0.02	0.01	0.01	0.01	0.02	0.01	0.01
Total	99.84	99.34	98.89	99.66	100.08	99.75	99.85	100.04	99.08	99.08
An content	40	48	59	54	37	42	50	57	41	41
Plagioclase microphenocrysts										
Sample	MIS-17-17M	MIS-17-17M	MIS-17-17M	MIS-17-17M	MIS-17-41F	MIS-17-41F	MIS-17-18M	MIS-17-18M	MIS-17-18M	MIS-17-18M
Crystal	plag 8	plag 8	plag 10	plag 10	plag 6	plag 6	plag 7	plag 7	plag 7	plag 8
Location	core	rim	core	rim	core	rim	core	rim	rim	core
SiO ₂	54.22	57.77	57.32	59.08	54.16	60.69	53.59	57.79	54.87	56.62
Al ₂ O ₃	29.17	26.51	27.15	26.07	28.90	25.06	29.02	26.22	28.46	27.57
FeO ^{Total}	0.24	0.21	0.26	0.23	0.23	0.19	0.46	0.30	0.51	0.37
MgO	0.01	0.01	0.01	0.01	0.01	0.00	0.04	0.01	0.04	0.02
CaO	11.54	8.15	9.04	7.86	10.93	7.06	11.54	7.91	10.75	9.66
Na ₂ O	4.43	6.30	5.93	6.27	4.89	6.72	4.53	6.45	4.82	5.57
K ₂ O	0.17	0.36	0.29	0.38	0.20	0.46	0.19	0.34	0.25	0.30
TiO ₂	0.01	0.01	0.03	0.00	0.01	0.01	0.03	0.01	0.03	0.01
Total	99.85	99.40	100.09	99.91	99.34	100.19	99.41	99.04	99.73	100.13
An content	58	41	45	40	55	36	58	40	54	48
Amphibole										
Sample	MIS-17-18M	MIS-17-18M	MIS-17-18M	MIS-17-18M	MIS-17-18M	MIS-17-18M	MIS-17-41C	MIS-17-41C	MIS-17-41C	MIS-17-41C
Crystal	am 3	am 3	am 3	am 5	am 5	am 5	am 1	am 1	am 1	am 1
Location	core	mid	rim	core	mid	rim	core	mid	rim	rim
SiO ₂	45.99	46.60	46.91	42.63	41.97	47.12	41.60	46.79	48.09	48.09
TiO ₂	1.29	1.27	1.23	1.94	2.18	1.20	2.31	1.23	1.53	1.53
Al ₂ O ₃	8.75	9.05	8.53	13.51	12.84	8.39	13.67	8.81	8.65	8.65
FeO ^{Total}	13.62	13.63	13.47	13.61	15.04	13.65	14.72	13.87	12.30	12.30
MnO	0.45	0.44	0.46	0.39	0.44	0.44	0.40	0.47	0.42	0.42
MgO	15.19	15.20	15.34	13.38	13.26	15.39	12.46	15.44	15.61	15.61
CaO	9.86	9.81	9.93	10.55	10.26	9.87	10.33	9.95	9.98	9.98
Na ₂ O	1.54	1.49	1.51	1.93	1.97	1.43	2.03	1.45	1.60	1.60
K ₂ O	0.39	0.38	0.39	0.61	0.62	0.38	0.66	0.39	0.47	0.47
Cl	0.08	0.07	0.06	0.05	0.03	0.08	0.05	0.07	0.06	0.06
Total	97.17	97.97	97.85	98.79	98.72	97.99	98.59	98.49	98.73	98.73

Table 1 (continued)

		Biotite								
Sample	MIS-17-17M	MIS-17-17M	MIS-17-17M	MIS-17-41C	MIS-17-41C	MIS-17-41C	MI16-01	MI16-01	MI16-01	
Crystal	bt 2	bt 2	bt 2	bt 1	bt 1	bt 1	bt 3	bt 3	bt 3	
Location	core	mid	rim	core	mid	rim	core	mid	rim	
SiO ₂	38.20	37.63	37.74	38.53	38.55	38.13	37.89	37.84	38.01	
TiO ₂	3.37	3.44	3.56	3.45	3.42	3.49	3.47	3.59	3.58	
Al ₂ O ₃	14.92	14.80	14.64	14.82	14.74	14.91	14.65	14.75	14.75	
FeO ^{Total}	14.40	14.36	14.64	14.04	13.93	13.19	14.20	14.34	13.56	
MnO	0.14	0.17	0.14	0.14	0.14	0.14	0.14	0.12	0.13	
MgO	15.23	15.30	15.53	15.17	15.14	15.64	15.12	15.30	15.49	
CaO	0.01	0.00	0.07	0.03	0.01	0.01	0.02	0.06	0.02	
Na ₂ O	0.67	0.68	0.71	0.67	0.66	0.72	0.60	0.62	0.63	
K ₂ O	8.04	8.01	7.58	7.87	7.84	7.72	7.90	7.90	7.95	
Cl	0.15	0.14	0.17	0.13	0.13	0.14	0.12	0.13	0.13	
F	0.18	0.17	0.19	0.17	0.16	0.17	0.19	0.15	0.15	
Total	95.28	94.70	93.69	95.00	94.72	94.25	94.32	94.80	94.39	
		Magnetite				Ilmenite				
Sample	MI16-01	MIS-17-41C	MIS-17-41F	MIS-17-18F	MIS-17-18M	MI16-01	MIS-17-41C	MIS-17-41F	MIS-17-18F	MIS-17-18M
SiO ₂	0.05	0.05	0.07	0.04	0.05	0.01	0.04	0.05	0.01	0.01
TiO ₂	5.27	5.20	5.71	5.35	5.38	31.42	33.22	27.99	29.09	29.89
Al ₂ O ₃	2.01	2.06	2.23	2.10	2.09	0.26	0.21	0.36	0.31	0.30
Cr ₂ O ₃	0.15	0.12	0.12	0.12	0.12	0.06	0.06	0.05	0.05	0.06
FeO ^{Total}	83.19	83.56	81.51	82.63	83.30	62.51	59.08	64.56	63.93	64.01
MnO	0.54	0.60	0.59	0.55	0.54	0.41	0.46	0.24	0.29	0.42
MgO	1.31	1.36	1.75	1.65	1.36	1.46	1.81	1.45	1.32	1.30
CaO	0.00	0.00	0.01	0.00	0.00	0.02	0.02	0.02	0.01	0.06
Total	92.56	93.01	92.02	92.50	92.90	96.15	94.92	94.72	95.06	96.05

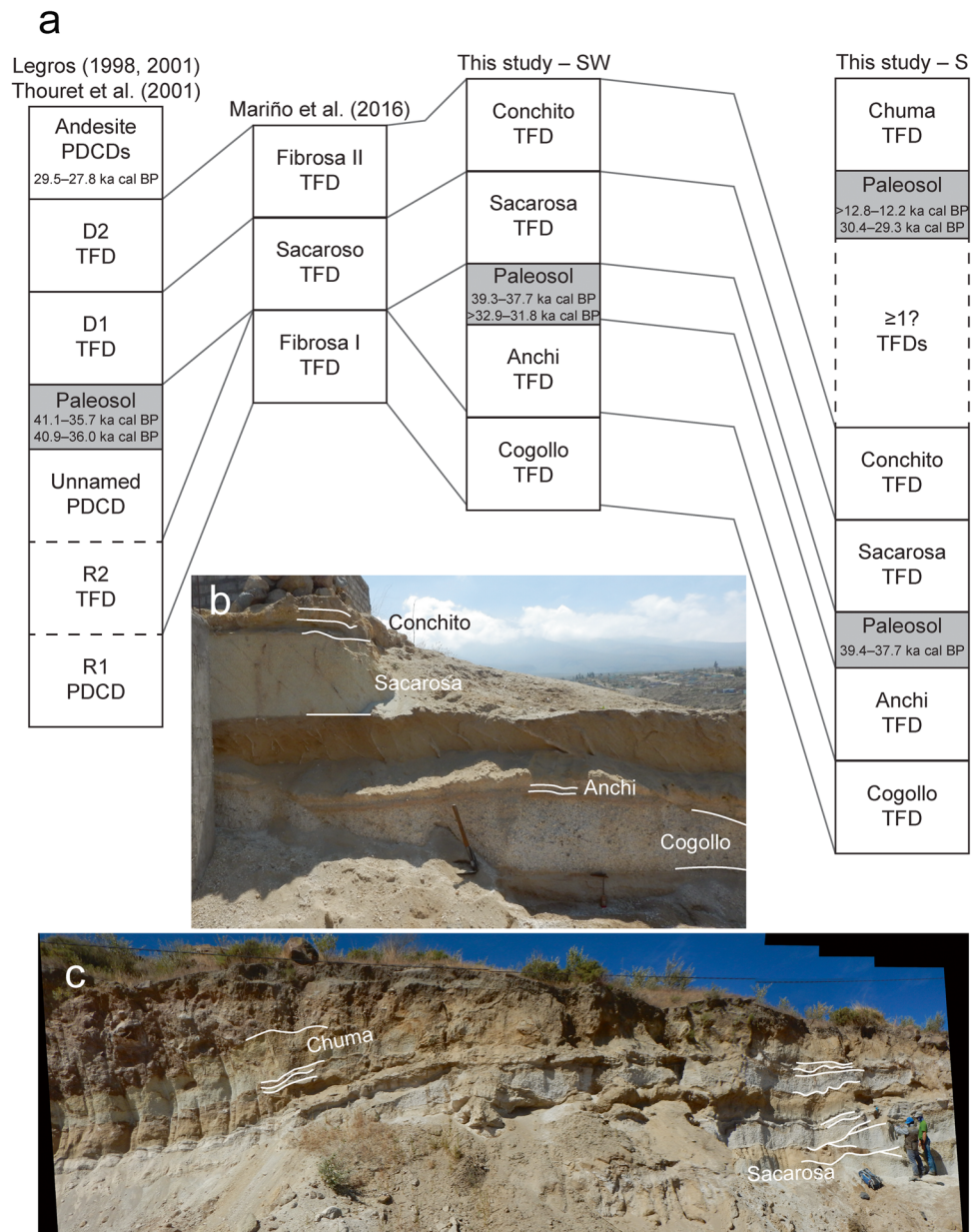
Typical 1 σ standard deviation for glass analyses (SiO₂ \pm 0.59, TiO₂ \pm 0.01, Al₂O₃ \pm 0.21, FeO^{Total} \pm 0.11, MnO \pm 0.02, MgO \pm 0.01, CaO \pm 0.10, Na₂O \pm 0.38, K₂O \pm 0.15, P₂O₅ \pm 0.01, Cl \pm 0.07); Typical 1 σ standard deviation for plagioclase analyses (SiO₂ \pm 0.44, Al₂O₃ \pm 0.17, FeO^{Total} \pm 0.02, MgO \pm 0.05, CaO \pm 0.08, Na₂O \pm 0.07, K₂O \pm 0.01, TiO₂ \pm 0.004); Typical 1 σ standard deviation for amphibole analyses (SiO₂ \pm 0.31, TiO₂ \pm 0.04, Al₂O₃ \pm 0.07, FeO^{Total} \pm 0.25, MnO \pm 0.02, MgO \pm 0.08, CaO \pm 0.06, Na₂O \pm 0.05, K₂O \pm 0.05, Cl \pm 0.004); Typical 1 σ standard deviation for biotite analyses (SiO₂ \pm 0.21, TiO₂ \pm 0.03, Al₂O₃ \pm 0.10, FeO^{Total} \pm 0.23, MnO \pm 0.02, MgO \pm 0.04, CaO \pm 0.004, Na₂O \pm 0.01, K₂O \pm 0.09, Cl \pm 0.005, F \pm 0.02); Typical 1 σ standard deviation for magnetite analyses (SiO₂ \pm 0.03, TiO₂ \pm 0.05, Al₂O₃ \pm 0.01, Cr₂O₃ \pm 0.004, FeO^{Total} \pm 0.35, MnO \pm 0.03, MgO \pm 0.01, CaO \pm 0.004); Typical 1 σ standard deviation for ilmenite analyses (SiO₂ \pm 0.02, TiO₂ \pm 0.39, Cr₂O₃ \pm 0.01, FeO^{Total} \pm 0.08, MnO \pm 0.08, MgO \pm 0.01, CaO \pm 0.003)

large ion lithophile elements (e.g., Rb, Ba, Th, K) and light rare earth elements (e.g., La, Ce), a depletion in heavy rare earth elements (e.g., Yb), and strong negative anomalies in high field strength elements (e.g., Nb). Type 1 pumice are slightly enriched in Rb (52–61 ppm) and Zr (173–179 ppm), and slightly depleted in Sr (535–593 ppm) compared to type 2 (Rb = 42–50 ppm, Zr = 144–156 ppm, Sr = 629–682 ppm).

Plagioclase compositions range from An₃₀ to An₆₄, with one core at An₇₁ (Fig. 5a; Table 1; ESM 7). Crystals range in size from 0.5 to 1.5 mm, have albite twinning, and are relatively inclusion free, blocky, and subhedral to euhedral. We define three end-member plagioclase populations which, in order of decreasing relative abundance, are (1) relatively simple plagioclase defined principally by oscillatory zoning, (2) plagioclase with one to two prominent resorption surfaces and calcic overgrowths,

and (3) subhedral to anhedral crystals with complex and patchy zoning (Fig. 6). A subset of the first two textures exhibits patchy and/or resorbed cores. Amphibole compositions range from magnesiohornblende to edenite and pargasite (Mg# ~ 0.62–0.69) (Fig. 5c, Table 1). Amphibole phenocrysts are 0.25–0.6 mm, generally subhedral to euhedral, exhibit both basal and diamond-shaped crystal forms, and display light green to medium brown pleochroism. Biotite phenocrysts occur as blocky, subhedral to euhedral crystals, range from 0.3 to 1.5 mm and exhibit light brown to medium brown pleochroism. Compositionally, the biotite phenocrysts are relatively Mg-rich (Mg# ~ 0.63–0.69) and plot in the biotite field nearest the siderophyllite end-member (Fig. 5b, Table 1). Amphibole and biotite lack reaction rims, while plagioclase and amphibole exhibit extension-cracked crystals,

Fig. 2 a Stratigraphic columns showing the Cayma stage deposits south and southwest of Misti with correlations to deposits in previous investigations. The stratigraphic columns are not to scale and do not represent the units' relative thicknesses or grain sizes. The stratigraphic positions of the dated paleosols and their ages are indicated. TFD is tephra-fall deposit and PDCD is pyroclastic-density-current deposit. **b** Typical outcrop southwest of Misti showing the Sacarosa TFD, associated Cayma stage units, and their stratigraphic positions. The shovel's handle is 50 cm. Charcoal from the paleosol underlying the Sacarosa TFD at this site was dated. **c** Outcrop south of Misti showing the Sacarosa TFD, Chuma TFD, intervening layers, and their stratigraphic positions. Contacts of individual Cayma stage tephra-fall deposits are highlighted. Charcoal and organic material from the paleosols beneath the Sacarosa and Chuma TFDs at this site were dated. Note the people on the right side of the outcrop for scale



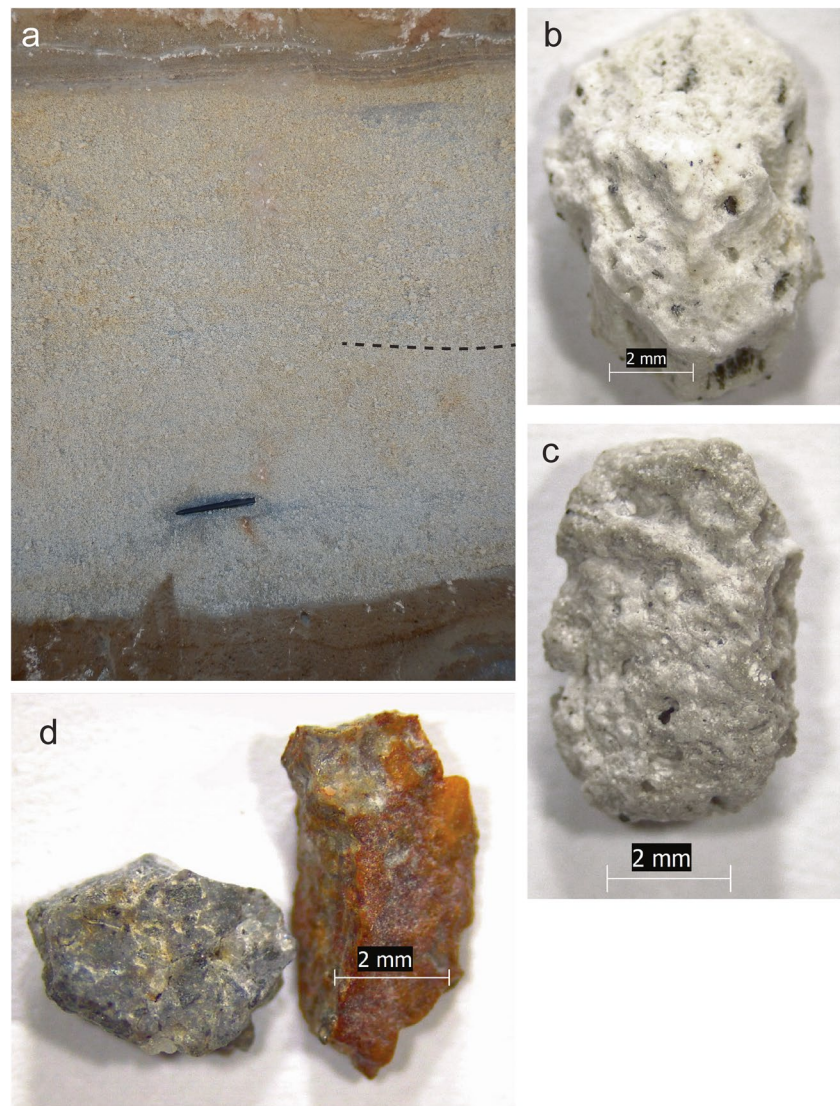
many of which contain interstitial melt fibers or foam (Fig. 6). Fe-Ti oxides compose ~ 1% of the pumice, with magnetite dominant and ilmenite sparse. Phenocrysts are subhedral, but exhibit both anhedral and euhedral crystal forms, ranging from 0.05 to 0.2 mm, with most ~ 0.1 mm.

The compositions of the Sacarosa pumice are within Misti's characteristic medium- to high-K calc-alkaline suite (2.0–2.3 wt.% K₂O; Fig. 4a) but exemplify one of the volcano's most differentiated magmas (Thouret et al. 2001; Rivera et al. 2017). The unit's trace-element concentrations (Fig. 4b) are also within Misti's normal range with characteristics typical of calc-alkaline continental margins (Grove and Kinzler 1986; Wilson 1989; Pearce and Peate 1995).

Magma conditions and ascent

Pre-eruptive magmatic conditions are determined with Putirka's (2016) amphibole-only and amphibole-melt thermobarometers and Ghiorso and Evans' (2008) Fe-Ti oxide thermometer and oxygen barometer. Putirka's (2016) amphibole-only and amphibole-melt thermometers yield temperatures well within uncertainty of each other. We approximate an amphibole temperature of 815 ± 30 °C and Fe-Ti oxide temperature of 799 ± 30 °C, consistent with oxide inclusions present throughout the amphiboles and the unit's dacitic composition. Ghiorso and Evans' (2008) oxygen barometer also indicates a fO₂ of Ni-NiO (NNO) + 1.5 (Table 4). Amphibole-melt pairs indicate the Sacarosa magma's pre-eruptive storage

Fig. 3 **a** Typical outcrop of Sacarosa tephra-fall deposit. Dashed line indicates the contact between the unit's upper and lower layers. Black pencil is 14 cm long. **b** Typical type 1 pumice. **c** Typical type 2 pumice. **d** Typical lithic types present in the deposit. These are exceptionally large examples



system was located at 310 ± 170 – 370 ± 160 MPa, or ~9–11 km depth (depths hereafter represent kilometers beneath Misti's summit; Fig. 7). Oxide pairs are in equilibrium according to Bacon and Hirschmann's (1988) criteria, and Putirka's (2016) test also shows amphibole-melt pairs are in equilibrium.

Sacarosa pumice textures indicate a rapid magma ascent rate typical of Plinian eruptions. The lack of reaction rims on amphibole and biotite phenocrysts are consistent with the inferred pressures at which amphibole last equilibrated, indicating that the magma did not linger at shallow depths prior to eruption. Additionally, the magma ascended sufficiently rapidly that microlites did not form and enough overpressure developed in decompressing melt inclusions to fracture their host phenocrysts (Fig. 6e). Melt fibers and foam filling the cracks in the phenocrysts indicate the process was syn-eruptive (Spieler et al. 2004; Kennedy et al. 2005; Miwa and Geshi 2012). The 1980 Mount St. Helens dacite ascended from similar depths in 4 h (Scandone and

Malone 1985; Endo et al. 1990) with decompression occurring sufficiently quickly that amphibole breakdown did not occur and the glass is microlite-free (Rutherford and Hill 1993). Experimental replication of such textures further indicates that they cannot exist if the magma takes more than a few hours to days to reach the surface (Rutherford and Hill 1993; Geschwind and Rutherford 1995). While we cannot currently quantitatively constrain the Sacarosa magma's ascent rate, such qualitative evidence and comparisons suggests that it rose from depth rapidly.

Distribution, volume, and column height

The Sacarosa TFD mantles the paleo-topography over more than 830 km^2 , thickening and coarsening toward Misti, its inferred source (Fig. 1). The unit's dispersal axis is southwest, similar to many of Misti's other TFDs (e.g., Legros

Table 2 Key characteristics for Sacarosa pumice types 1 and 2

Characteristic	Type 1	Type 2
Color	White	Gray
Average proportion of deposit > 2 mm	83 wt. %	10 wt. %
Average density ^a	500 kg/m ³	800 kg/m ³
Vesicle content	50–60 vol. %	60 vol. %
Groundmass glass content	25–30 vol. %	30–35 vol. %
Phenocryst (> 0.5 mm) and microphenocryst (0.1–0.5 mm) content	10–15 vol. %	5–10 vol. %
Plagioclase	3–6 vol. %	3–6 vol. %
Amphibole	3–5 vol. %	3–5 vol. %
Biotite	1–3 vol. %	trace
Fe-Ti oxides	< 1 vol. %	< 1 vol. %
Vesicles size populations	Bimodal; (0.05–1 mm) and (1–3 mm)	Unimodal; (0.05–1 mm)
Microvesicle (0.05–1 mm) shapes	subrounded to rounded	subrounded to rounded
Vesicle (1–3 mm) shapes	Complex and irregular	
Domains of deformed glass and vesicles	Uncommon	

^aDetermined by Houghton and Wilson's (1989) method

2001; Cacya et al. 2007; Harpel et al. 2011). The thinnest Sacarosa deposit that we document along its dispersal axis is 24 cm, implying that the unit was emplaced over a much wider area than our data indicates. We did not observe the Sacarosa unit east of *Quebrada* (Spanish for ravine) San Lazaro despite thicknesses over 100 cm just west of the channel (Fig. 1b). East of the *quebrada*, erosion removed it, or younger deposits buried it.

The Sacarosa TFD's thickness and distribution permit only four isopachs at 40 cm or thicker (Fig. 1b; ESM 8). Plotting deposit thickness versus square root of the area enclosed within each isopach ($A^{1/2}$) yields a single line segment, from which Pyle (1989) and Fierstein and Nathenson's (1992) method provides a minimum bulk volume of 0.4 km³ (Table 4). Bonadonna and Costa's (2012, 2013) Weibull method using Daggitt et al.'s (2014) application yields a similar volume of 0.3 km³.

The crystal enrichment and scant fine vitric material in our Sacarosa samples indicate that its eruption generated a significant amount of fine ash that was deposited downwind of the mapped area. Its minimum volume excludes such fine ash, which can account for a significant proportion of a deposit's volume (Walker 1980; Rose 1993; Bonadonna et al. 1998). Estimating volumes for deposits like the Sacarosa TFD, which lack distal isopachs is challenging. Bonadonna and Houghton's (2005) method accounts for such distal ash, yielding a bulk volume of 1.7 km³ using proximal (*B*) and distal (*C*) integration limits of 1 and 1000 km, respectively. Their method, however, is sensitive to integration limits and problematic for deposits like the Sacarosa TFD, which lack proximal and distal isopachs, leading to uncertainty

in the resulting volume (Sulpizio 2005; Bonadonna and Costa 2013; Biass et al. 2019).

Well-preserved TFDs yield multiple line segments on \log_{10} of the deposit thickness versus $A^{1/2}$ plots (Rose 1993; Bonadonna et al. 1998). The Sacarosa data, however, only define a single line segment on such plot (ESM 8), but the distal segment representing the fine ash distributed far from the vent is notably absent. We apply Sulpizio's (2005) method to estimate that the inflection point between the deposit's proximal line segment, which is defined by our data, and its distal segment, for which we lack data, is located at $A^{1/2} = 20$ km and 23 cm thickness. The distal line segment's slope is further estimated to be $k = 0.0749 - 0.0142$ using Sulpizio's (2005) Eqs. 5–7. Using such slopes with the inflection point, Fierstein and Nathenson's (1992) method for calculating deposit volume from multiple line segments yields a volume of 0.6–3.2 km³. The lower value's similarity to the unit's minimum volumes derived from the other methods indicates that it does not represent the deposit's complete volume. Such lower values also underestimate the volume of deposits with less than 70% of their bulk volume in proximal areas (Sulpizio 2005). Considering the evidence for abundant fine ash produced during the Sacarosa eruption, it is reasonable to expect that more than 30% of the deposit's volume was emplaced distally. Additionally, the Sacarosa TFD thickness and distribution are similar to those of other eruptions with bulk volumes from 1 to 10 km³ (e.g., Sarna-Wojcicki et al. 1981; Scasso et al. 1994; Fontijn et al. 2011), and the unit is significantly thicker and more widely dispersed than Misti's 2-ka TFD (ESM 8), which has a minimum volume of 0.2–0.6 km³ and

Table 3 Whole-rock geochemistry for Sacarosa pumice

Sample Pumice Type	MIS-16-08c ^a Type 1	MIS-16-08f [†] Type 2	MIS-17-18f [†] Type 2	MIS-17-18c ^a Type 1	MIS-17-41c ^a Type 1	MIS-17-41f [†] Type 2	MII7-02 ^a Both	MII5-21 ^b Both	MII6-01 ^b Both	I.27 ^c	MI1 ^c
Analytical Technique XRF											
Major elements (wt%)											
SiO ₂	62.98	61.66	61.81	62.81	63.00	60.91	62.51	62.56	62.94	64.53	65.49
TiO ₂	0.623	0.613	0.588	0.611	0.635	0.584	0.571	0.6	0.587	0.57	0.58
Al ₂ O ₃	14.94	16.26	16.31	15.56	15.03	16.13	16.39	16.26	15.55	16.23	15.62
Fe ₂ O ₃ ^{Total}	4.81	4.21	4.46	4.65	4.88	4.04	4.11	4.68	4.43	5.07	5.15
FeO ^{Total}	0.10	0.096	0.093	0.1	0.105	0.094	0.09	0.101	0.095	0.09	0.1
MnO	2.22	2.34	2.22	2.22	2.28	2.31	2.05	2.13	2.07	2.39	2.36
MgO	3.67	4.4	4.4	3.96	3.72	4.37	4.19	4.18	3.96	4.5	4.03
CaO	3.58	3.77	4.05	3.86	3.76	3.87	4.06	3.75	3.73	3.95	3.77
Na ₂ O	2.89	2.54	2.44	2.67	2.77	2.42	2.53	2.47	2.62	2.62	2.86
K ₂ O	0.235	0.227	0.22	0.231	0.241	0.23	0.225	0.262	0.219	0.423	0.474
P ₂ O ₅	2.86	3.21	3.02	2.27	2.67	3.99	2.66	2.96	2.96		
LOI	98.92	99.33	99.61	98.95	99.09	98.94	99.39	97.00	99.16	100.37	100.43
Volatiles (wt.%)											
F ≥	b.d.	b.d.	0.01	0.06	0.02	b.d.	b.d.				
Cl ≥	0.06	0.03	0.05	0.06	0.08	b.d.	0.06				
SO ₃ ≥	0.03	0.04	0.04	0.05	0.1	0.14	0.01				
Trace elements and volatiles (ppm)											
Ni	15	15	18	13	15	16	14	18	15	134	175
Cr	28	34	40	26	28	34	27	30	29	33	27
V	96	93	91	92	98	85	85	93	95	103	106
Sc	10	10	10	8	9	11	9	9	8	9	9
Cu	20	43	45	13	20	61	43	37	19	24	29
Zn	76	71	73	76	76	71	77	77	70	76	92
Ga	17	15	20	18	18	16	19	19	19		
Ba	1083	977	1004	1039	1092	1131	1040	942	1072	965	1124
Rb	61	46	50	55	56	42	51	54	53		
Sr	535	629	682	593	544	638	668	654	619	645	591
Y	15	11	14	15	16	14	12	13	14	14	14
Zr	179	151	156	173	177	144	174	177	173	177	200
Hf	4	5	3	3	4	4	5				
Nb	9	8	9	8	9	7	7	8	7		
Mo	1	2	2	1	1	2	1				

Table 3 (continued)

Sample Pumice Type	MIS-16-08c ^a		MIS-16-08f ^a		MIS-17-18f ^a		MIS-17-18c ^a		MIS-17-41c ^a		MIS-17-41f ^a		MI17-02 ^a		MI15-21 ^b		MI16-01 ^b		MI1 ^c
	Type 1	Type 2	Type 2	Type 1	Type 2	Type 1	Type 1	Type 1	Type 1	Type 2	Both	Both	Both	Both	Both	Both	Both	Both	
La	30	31	29	28	29	32	32	38	32	32	32	32	30	34	34	28.2	30.1		
Ce	61	59	62	59	62	66	66	54	59	59	59	62	62	67	67	62.8	77.7		
Nd	24	28	27	23	27	29	29	25	25	25	25	26	26	30	30				
Sm	4		5	4	5	5	5		4	4	4								
Dy	3		3	3	3	3	3		2	2	2								
Yb	2		2	3	2	2	2		1	1	1								
Th	5	6	4	5	4	6	6	5	5	5	5	6	6	4	4				
Pb	15	17	15	16	15	14	14	18	16	16	16	18	18	16	16				
Br ≥	1	4	1	2	1	4	4	5	2	2	2								
As ≥	b.d.	2	3	b.d.	3	2	2	4	b.d.	4	b.d.								
Analytical Technique ICP-MS																			
Trace elements (ppm)																			
Ag	0.05		0.07	0.04				0.04											
Ba	1055		1048	1022				1022						1081					
Bi	0.05		0.05	0.05				0.05											
Cd	0.09		0.08	0.05				0.05											
Cr	29.3		40.2	28.1				28.1											
Cs	1.24		1.02	1.09				1.09						1.02					
Ga	18.5		19.6	19.1				19.1											
Ge	1		1.3	1.2				1.2											
Hf	4.56		4.17	4.37				4.37						4.42					
Mo	1.38		1.36	1.2				1.2											
Nb	7.54		6.79	6.98				6.98						7.26					
Pb	16.7		16.1	15.8				15.8						16.34					
Rb	59.5		49.6	52.4				52.4						53.5					
Sb	0.29		0.31	0.33				0.33											
Sc	8.3		10.1	8.7				8.7						9.3					
Sn	1.6		1.37	1.4				1.4											
Ta	0.47		0.43	0.43				0.43						0.44					
Th	4.44		4.06	4.19				4.19						4.46					
Tl	0.21		0.21	0.18				0.18											
U	0.53		0.5	0.49				0.49						0.6					
V	99		97	98				98											
Y	12.8		11.6	12.2				12.2						14.06					

Table 3 (continued)

Sample	MIS-16-08c ^a	MIS-16-08f ^a	MIS-17-18f ^a	MIS-17-18c ^a	MIS-17-41c ^a	MIS-17-41f ^a	MI17-02 ^a	MI15-21 ^b	MI16-01 ^b	MI1 ^c
Pumice Type	Type 1	Type 2	Type 2	Type 1	Type 1	Type 2	Both	Both	Both	MI1 ^c
Zn	78	72	73							
Sr									636	
Zr									170	
La	31.46	30.25	29.92						34.79	
Ce	63.9	61.44	61.67						64.63	
Pr	7.07	6.7	6.74						7.69	
Nd	26.31	24.99	24.8						28.76	
Sm	4.31	4.11	4.13						4.84	
Eu	1.01	1.15	1.04						1.24	
Gd	3.33	3.1	3.21						3.64	
Tb	0.46	0.42	0.44						0.51	
Dy	2.45	2.38	2.4						2.84	
Ho	0.46	0.43	0.45						0.53	
Er	1.21	1.2	1.16						1.39	
Tm	0.18	0.18	0.18						0.2	
Yb	1.17	1.1	1.16						1.25	
Lu	0.18	0.17	0.18						0.19	

Blank indicates not analyzed or not reported. Marked with b.d. indicates analyzed but below detection limits

^aAnalysis at Hamilton Analytical Lab. Typical average analytical errors at 1σ for XRF analysis of major elements (wt.%) is SiO₂ (0.17), TiO₂ (0.01), Al₂O₃ (0.08), FeOTotal (0.08), MnO (0.002), MgO (0.04), CaO (0.04), Na₂O (0.05), K₂O (0.02), P₂O₅ (0.005); XRF analysis for trace elements (ppm) are As (3), Ni (2), Cr (3), V (3), Sc (0.8), Cu (2), Zn (3), Ga (1), Ba (13), Rb (1), Cs (2), Sr (8), Y (1), Zr (5), Hf (0.5), Nb (0.8), Ta (1), Mo (1), La (2), Ce (4), Nd (2), Sm (0.4), Dy (0.3), Yb (0.7), Th (1), U (1), Pb (2), Bi (1); and LA-ICP-MS analysis of trace elements at 2σ are Ag (0.02), Ba (16), Bi (0.02), Cd (0.02), Cr (3.2), Cs (0.04), Ga (0.4), Ge (0.1), Hf (0.14), Mo (0.12), Nb (0.23), Pb (0.7), Rb (1.0), Sb (0.07), Sc (0.2), Sn (0.11), Ta (0.02), Th (0.13), Tl (0.03), U (0.03), V (1), Y (0.3), Zn (3), La (0.50), Ce (1.07), Pr (0.10), Nd (0.55), Sm (0.15), Eu (0.03), Gd (0.13), Tb (0.02), Dy (0.08), Ho (0.02), Er (0.06), Tm (0.01), Yb (0.06), Lu (0.01)

^bAnalysis at Washington State University GeoAnalytical Lab

^cFrom Legros (1998)

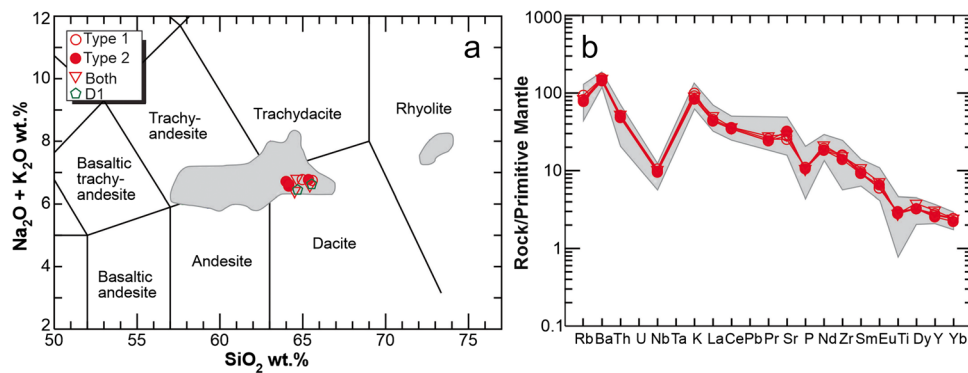


Fig. 4 Major and trace element concentrations of the Sacarosa pumice compared with Misti's other eruptive products (gray field) from the past 120 ky (Rivera et al. 2017). **a** Total alkali-silica diagram (Le Bas et al. 1986) showing the Sacarosa pumice's dacitic composition,

an estimated total bulk volume of 1.4 km³ (Harpel et al. 2011; Cobeniñas et al. 2012). As a result, the higher value of about 3 km³ better represents the Sacarosa TFD's bulk volume.

Sacarosa PDC deposits would also increase the deposit's bulk volume, but such deposits associated with the Sacarosa eruption are yet to be identified. While large-magnitude eruptions that do not produce PDCs are documented (Williams and Self 1983; Fontijn et al. 2011; Harpel et al. 2019), they are rare, and at least 70% of Plinian eruptions do generate such phenomena (Newhall and Hoblitt 2002). Multiple Cayma stage PDC deposits crop out (Legros 2001; Thouret et al. 2001; Mariño et al. 2016), but only the R1 deposit is correlated to its eruption. Due to the presence of such non-correlated Cayma stage PDC deposits, future investigation may reveal that one or more are co-genetic with the Sacarosa TFD and would increase the unit's bulk volume.

We convert bulk to dense rock equivalent (DRE) volume by assuming typical TFD bulk densities of 800–1000 kg/m³ (Walker 1981; Sparks et al. 1997) to calculate the unit's mass. We then use a rock density of 2400 kg/m³ to convert the unit's mass to a DRE volume of 1.1–1.3 km³ (Table 4). The dearth of lithics precludes needing to remove accidental material from the DRE volume.

Applying Carey and Sparks' (1986) method to the pumice isopleth data (ESM 8) yields an eruption column neutral buoyancy height (H_U) of 14–21 km above the crater and winds of ~10–20 m/s. Sulpizio's (2005) empirical relation of k to maximum column height (H_T) yields a similar value of 18 km above the crater. Pumice, especially large clasts, often break upon impact skewing resulting column heights (Bonadonna et al. 2013), but the Sacarosa TFD is relatively fine grained and few of its pumice appear broken. Sparks' (1986) empirical relationship between H_U and H_T and adjustment for Misti's

subtle compositional differences between pumice types, and overlap with Legros' (1998) D1 deposit. **b** Trace element concentrations of the Sacarosa pumice normalized to primitive mantle after Sun and McDonough (1989)

elevation (~6 km asl) indicates that the maximum column height reached 24–36 km asl (Table 4) during the Sacarosa eruption.

Eruption dynamics

The textural homogeneity of each of the Sacarosa TFD's layers indicates steady eruption and wind conditions during emplacement of each, but the increase in grain size from the Sacarosa deposit's lower to upper layer implies a shift to either more vigorous eruption conditions or a lesser degree of fragmentation. Changing wind direction is not the cause of the up-section coarsening since the layers are of about equal thickness throughout the unit's distribution. The diffuse contact between layers and lack of evidence for a time break indicate emplacement by a single continuous eruption.

Within 15–20 km from the vent, the Sacarosa TFD's < 1 mm size fraction composes 50–80 wt.% of the deposit, which is a degree of fragmentation commonly associated with phreatomagmatism. Such an eruption mechanism, however, is excluded by the unit's sorting (< 1.75; ESM 3), scarcity of lithics, and paucity of fine vitric ash in proximal areas (Walker 1973; Gonnermann 2015; Houghton and Carey 2015). High overpressure, induced by the rapid ascent of the Sacarosa magma, correlates to fragmentation efficiency and can produce fine-grained deposits (Kueppers et al. 2006). The abundance of loose crystals lacking adhering glass and sub-angular to sub-rounded pumice also indicates secondary fragmentation that would further reduce grain-size (Jones et al. 2016). The inferred vigor of the Sacarosa eruption, its column height, and its bulk volume all indicate a VEI 5 Plinian event (Newhall and Self 1982), confirming Mariño et al.'s (2016) initial assessment.

Mass discharge rates correlate to column height (Sparks 1986; Sparks et al. 1997; Mastin et al. 2009). Applying

Fig. 5 Mineral composition and classification diagrams. **a** Histogram of plagioclase phenocryst and microphenocryst An content. **b** Biotite classification after Rieder et al. (1998). **c** Calcic amphibole classification applying Leake et al.'s (1997) definitions based on $(\text{Na} + \text{K})_A$ contents. Amphibole represented by gray triangles are classified according to the names listed in gray, whereas those represented by black circles correspond to names in black. Biotite and amphibole parameters are given in atoms per formula unit (apfu)

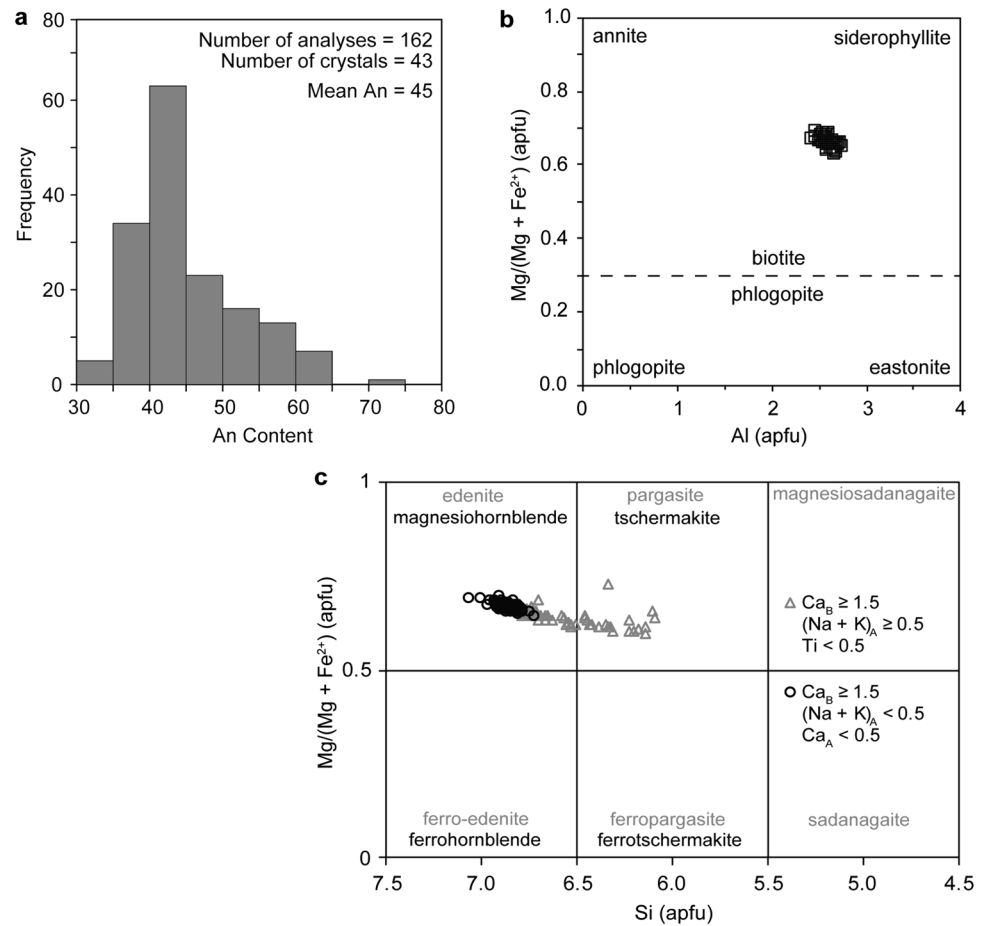


Fig. 6 Representative back-scattered electron images of the Sacarosa plagioclase's end-member types (**a–c**) and an extension-cracked plagioclase crystal (**d**). **a** Oscillatory zoned crystals; **b** subhedral to anhedral crystals with patchy, complex zoning; **c** crystals with resorption surfaces followed by calcic overgrowth; **d** an extension-cracked crystal with melt fibers (yellow arrows) that bridge the crack. White box in **c** indicates the portion of the crystal shown in **d**. Scale bars are 250 μm

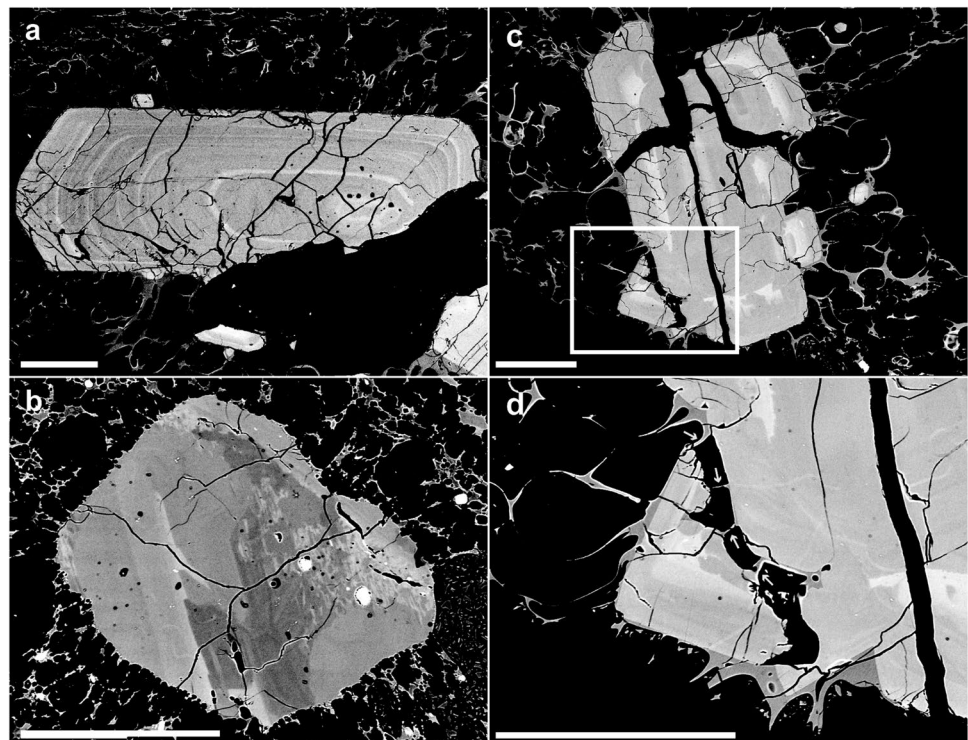


Table 4 Key characteristics of the Sacarosa tephra-fall deposit and its eruption

Characteristic	Inferred or measured value
Composition	Dacite
Glass composition	62–66 wt.% SiO ₂ , 69–75 wt.% SiO ₂
Plagioclase composition	An _{30–64, 71} ; Average An ₄₅
Amphibole classifications	Pargasite, edenite, magnesiohornblende
Pumice 1 density (ρ_1) ^a	500 kg/m ³
Pumice 2 density (ρ_2) ^a	800 kg/m ³
Pumice vesicularity	50–60%
Crystal proportions in pumice	plg (3–6%); amph (3–5%); bt (1–3%); ox (~1%)
Magma temperature ^{b,c}	799–815 °C
Log ₁₀ fO ₂ (relative to NNO) ^b	+ 1.5
Minimum bulk volume ^{d,e,f}	0.3–0.4 km ³
Bulk volume ^{e,g}	3.2 km ³
DRE Volume ^h	1.1–1.3 km ³
Total deposit mass ^h	2.6–3.2 × 10 ¹² kg
H _u ^{g,i}	14–21 km above vent
H _T ^{ij}	24–36 km asl
Volume (DRE) eruption rate ^k	3.2 × 10 ³ –1.7 × 10 ⁴ m ³ /s
Mass eruption rate ^l	7.7 × 10 ⁶ –4.1 × 10 ⁷ kg/s
Eruption duration ^m	Tens of hours
Wind speed ⁱ	10–20 m/s
Dispersal axis	Southwest
Eruption classification ⁿ	Plinian
Volcanic Explosivity Index ⁿ	5

^aHoughton and Wilson's (1989) method^bGhiorso and Evans' (2008) method^cPutirka's (2016) method^dPyle's (1989) method^eFierstein and Nathenson's (1992) method^fBonadonna and Costa's (2012, 2013) method^gSulpizio's (2005) method^hAssuming deposit density of 800–1000 kg/m³ⁱCarey and Sparks' (1986) method^j6 km added for crater elevation^kMastin et al.'s (2009) method^lAssuming ρ_{magma} of 2400 kg/m³^mFrom MER and DRE volume and comparison with analog eruptionsⁿNewhall and Self's (1982) method

Mastin et al.'s (2009) empirical relation to our column height yields mass eruption rates (MER) of 7.7×10^6 – 4.1×10^7 kg/s, assuming a magma density of 2400 kg/m³. For the Sacarosa TFD's DRE volume, a MER of this magnitude implies an eruption duration between 17 h and five days. A comparison with other eruptions of similar volume (e.g., Rose 1972; Fierstein and Hildreth 1992; Hildreth and Drake 1992), however, indicates that a duration of several days is unlikely. Our minimum duration assumes peak discharge conditions

throughout the eruption because our MER is based upon maximum column height, which is inferred from isopleth data. The unit's isopleth data and its derivative MER, however, more likely represent the eruption conditions during emplacement of the unit's coarse upper layer, while the finer grain size of the lower layer suggests emplacement by a lower eruption column height and MER. Consequently, the eruption likely took longer than our minimum duration and as a result, we infer that it lasted for tens of hours (Table 4).

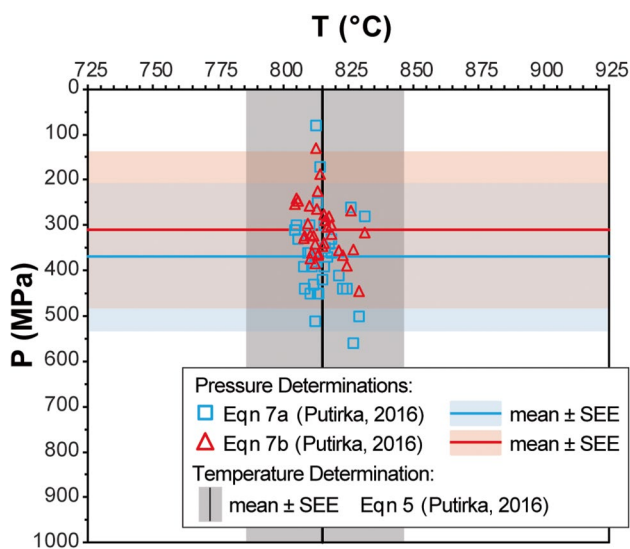


Fig. 7 Pressure and temperature (P–T) determinations using Putirka's (2016) amphibole-only and amphibole-melt thermobarometric equations. Open symbols show P–T determinations for individual amphibole-melt pairs using two different pressure equations. The mean P–T from 34 amphibole-melt pairs for the respective equation used are indicated by a solid line, and the corresponding expected standard error of estimate for each method is shown by a shaded region

Age

We constrain the Sacarosa TFD's emplacement with ages from overlying and underlying units within our Bayesian model developed in OxCal (Bronk Ramsey 2009). By incorporating stratigraphic relations as independent information, the model can refine calibrations and statistically determine the age of the Sacarosa TFD and associated Cayma stage TFDs with 95.4% confidence based on their stratigraphic positions among each other and the available ages. Within the model, queries can also be performed to statistically determine the length of time between events or determine the probable sequence of events where stratigraphic relations are not known (Bronk Ramsey 2009). For our model and a detailed explanation of its components, see ESM 1.

Charcoal samples collected in this study from the paleosol underlying the Sacarosa TFD yielded ages of 39.3–37.7 ka cal BP (all calibrated ages reported at 95.4% confidence) and 39.4–37.7 ka cal BP. In contrast, humic acids from organic material provided an age of 32.9–31.8 ka cal BP (Table 5; Harpel et al. 2023). Legros (1998, 2001) and Thouret et al. (1996, 1999, 2001) reported two additional ages of 41.1–35.7 ka cal BP and 41.0–36.0 ka cal BP, respectively, from the paleosol underlying the Sacarosa TFD. All the ages from the paleosol underlying the Sacarosa TFD are statistically indistinguishable except our humic acids age (ESM 1), which typically yield minimum ages representing

the component's average residence time rather than a deposit's emplacement age (Trumbore 2000).

Organic material and microcharcoal from the reworked layer beneath the Chuma TFD, which overlies the Sacarosa TFD, yielded ages of 30.4–29.3 ka cal BP and 12.8–12.2 ka cal BP, respectively, providing minimum age constraint. A third minimum age constraint is 29.5–27.8 ka cal BP (Legros 2001; Thouret et al. 2001) from a deposit stratigraphically above the Sacarosa TFD and other Cayma stage deposits. An additional age of 39.5–33.3 ka cal BP ostensibly provides a minimum age for the Cayma stage (Legros 2001; Thouret et al. 2001), but the unit it was derived from only has a direct overlapping relation with the Cogollo TFD (Legros 1998), while its relations with other Cayma stage units, including the Sacarosa TFD, are not known. As a result, we use it in our model to constrain the Cogollo TFD's minimum age rather than the entire Cayma stage. Using such constraints within our Bayesian age model, we infer that the Sacarosa TFD was emplaced between 38.5 ka cal BP and 32.4 ka cal BP.

Implications of the Sacarosa TFD

Timing, quantity, and magnitude of explosive Cayma stage eruptions

By applying the Sacarosa TFD as a marker bed, it becomes apparent that multiple Cayma stage TFDs delineate a more complex period of explosive volcanism than just the deposits from the three eruptions described by Legros (2001) and Mariño et al. (2016). Our preliminary investigation reveals deposits from at least five and perhaps six or more explosive eruptions during the stage (ESM 2). The first documented Cayma stage eruption emplaced the Cogollo tephra-fall and PDC deposits, while the Sacarosa TFD was produced by the third event (Fig. 2). Overlapping relations suggest at least one more unnamed TFD likely crops out between the Conchito and Chuma deposits. The TFD dated by Ayala-Arenas et al. (2019) crops out individually and its stratigraphic relation with the other Cayma stage deposits is not directly observed. Nonetheless, its age indicates that it is not the Cogollo TFD and was likely emplaced between the Anchi and Chuma TFDs (ESM 1).

Our modeling of new and published ^{14}C ages indicates that the Cayma stage deposits were emplaced during a period of explosive volcanism beginning perhaps as early as 44.9 ka cal BP and lasting about 8.9–15.5 ky (ESM 1). The Cogollo TFD was emplaced sometime from 44.9 to 38.7 ka cal BP by the stage's first eruption, which was followed by the Anchi (43.2–38.3 ka cal BP), Sacarosa (38.5–32.4 ka cal BP), and Conchito (37.1–30.5 ka cal

Table 5 Radiocarbon and modeled ages for the Cayma stage deposits

Sample/ Unit	Lab Code	Location	Method	Material	Deposit	Pre-treatment	Conventional ¹⁴ C Age (BP; 1σ)	δ ¹³ C (‰)	Modeled Age Range (cal BP; 95.4%)	Sacaroza Constraint	Reference
MII 7-06	PR1-6801/ UGAMS- 58009	16.362°S 71.497°W	AMS	micro-char- coal	paleosol	acid/alkali/ acid	10,640 ± 100	-27.4	12,763– 12,174	minimum	This study; Harpel et al. (2023)
	GrN-23889	Huarangal/ Huarangeras	Conventional	charcoal	tephra-fall deposit		20,960 ± 380/360 (370)		25,923– 24,286		Thouret et al. (2001)
	GrN-23247	Pastores	Conventional	charred wood	block-and- ash-flow deposit		24,840 ± 475/480 (478)		29,466– 27,820	minimum	Legros (1998; 2001); Thouret et al. (2001)
MII 7-05	Beta-470309	16.362°S 71.497°W	AMS	organic mate- rial	paleosol	acid/alkali/ acid	25,620 ± 220	-21.7	30,371– 29,327	minimum	This study; Harpel et al. (2023)
MII 5-23	WW-10535	16.341°S 71.496°W	AMS	humic acids	paleosol	acid	28,160 ± 100	-24	32,845– 31,745		This study; Harpel et al. (2023)
	GrN-23246	Grande- Honda	Conventional	charcoal	block-and- ash-flow deposit		31,200 ± 1,330		39,489– 33,263		Legros (1998, 2001); Thouret et al. (2001)
MII 6-133	Beta-455170	16.301°S 71.522°W	AMS	charcoal	paleosol	acid/alkali/ acid	33,690 ± 230	-23.5	39,266– 37,691	maximum	This study; Harpel et al. (2023)
MII 7-09	Beta-470310	16.362°S 71.497°W	AMS	charcoal	paleosol	acid/alkali/ acid	33,780 ± 250	-23.5	39,362– 37,712	maximum	This study; Harpel et al. (2023)
	GrN-21574	Pastores	Conventional	organic mate- rial	paleosol		33,870 ± 1,800/1,460 (1630)		40,913– 36,009	maximum	Thouret et al. (1996, 2001)
		Pastores	Conventional?	charcoal	paleosol		34,000 ± 2,000		41,076– 35,728	maximum	Legros (1998, 2001)
	GrN-23884		Conventional	charcoal	pyroclastic- density current		40,200 ± 820/740 (780)		44,573– 42,552		Thouret et al. (2001)
Cogollo			Modeled						44,895– 38,663		This study
Anchi			Modeled						43,155– 38,333		This study
Sacaroza			Modeled						38,458– 32,360		This study
Conchito			Modeled						37,047– 30,482		This study

Table 5 (continued)

Sample/ Unit	Lab Code	Location	Method	Material	Deposit	Pre-treatment	Conventional ^{14}C Age (^{14}C BP; 1 σ)	$\delta^{13}\text{C}$ (‰)	Modeled Age Range (cal BP; 95.4%)	Sacarosa Constraint	Reference
TL-dated unit			TL/Modeled						34,567–28,738		Ayala-Arenas et al. (2019); This study
Chuma			Modeled						30,255–28,751		This study

Blank fields represent no data reported. For ages with reported asymmetrical analytical error, the value in parentheses used for calibration

BP) eruptions. Subsequent Cayma stage eruptions possibly emplaced multiple unnamed TFDs and culminated with the Chuma eruption about 30.3–28.8 ka cal BP.

The Sacarosa TFD is the first of the Cayma stage's units to be described in detail and its eruption characterized. It is both the third most voluminous eruption in the CVZ and Misti's most voluminous eruption yet documented. Other Cayma stage TFDs erupted during Misti's phase of explosive silicic eruptions are of comparable thicknesses and distributions to the Sacarosa TFD, implying eruptions of similar volume and explosivity (Legros 2001; Mariño et al. 2016). Additionally, several Cayma stage deposits, including the Cogollo and Sacarosa TFDs are thicker and more widely distributed than many of Misti's younger, andesitic units (Legros 2001; Harpel et al. 2021). Up to six or more deposits emplaced in perhaps 8.9–15.5 ky indicate a period of particularly intense explosive volcanism at Misti.

Post-Cayma stage eruption magnitudes

Of Misti's more recent late Pleistocene and Holocene andesitic deposits, the Autopista, Pampa de los Huesos, and possibly Sandwich Inferior TFDs (Cacya et al. 2007; Escobar 2021; Harpel et al. 2021) are of sufficiently comparable thicknesses and distributions to the Sacarosa TFD to infer emplacement by similarly powerful and voluminous eruptions.

The Sacarosa TFD clearly represents a more voluminous and powerful eruption than many of Misti's other post-Cayma stage TFDs, including the 2-ka TFD (ESM 8), indicating that VEI 5 eruptions do not occur at the frequency they did during emplacement of the Cayma stage deposits. Younger analogous TFDs, nonetheless, imply that despite its lack of characterized eruptions and historical slumber, Misti can still produce powerful paroxysmal explosive events, and the volcano's eruption history should reflect this. Recent investigations at Ubinas, Sara Sara, and Yucamane-Calientes volcanoes, Peru (e.g., Wright et al. 2018; Rivera et al. 2020a, b), and Cerro Blanco Caldera, Argentina (Fernandez-Turiel et al. 2019), further illustrate that VEI 5 or greater eruptions are also probably more common at volcanoes throughout Peru and the CVZ than previously documented.

Magma genesis and ascent

Deposits from Misti that are older than the Cayma stage are compositionally similar to deposits subsequent to the Cayma stage (Thouret et al. 2001; Rivera et al. 2017). Such deposits indicate that Misti's magmatic evolution is more complex than Legros' (2001) rhyolite-dacite-andesite progression. While unlikely, were such a compositional shift to biotite-bearing silicic magmas to recur at Misti, it could herald the onset of thousands of years of intense, explosive activity.

The Sacarosa eruption's parent magma likely followed Misti's normal magmatic path, experiencing assimilation-fractional crystallization processes between its mantle source and ~ 10 km-depth magma chamber (Mamani et al. 2010; Rivera et al. 2017). This depth is similar to those inferred for other eruptions at Misti (Ruprecht and Wörner 2007; Tepley et al. 2013; Takach et al. in review), indicating that it is a typical magma storage level. Once there, it continued evolving for an unknown period into one of Misti's more silicic magmas. While resorption surfaces and complex zoning in some Sacarosa plagioclase record convection and intrusions into the magma chamber, the event that triggered ascent of the Sacarosa magma remains unidentified. Preliminary petrologic evidence additionally indicates some differences in magmatic conditions may exist among the adjacent Cayma stage units (Topham et al. 2021), indicating that they likely experienced slightly different evolutionary paths leading to eruption.

The Sacarosa magma rose from its ~ 10-km-deep chamber rapidly, culminating in the paroxysmal eruption. Misti's 2-ka eruption also resulted from magma ascending from a similar depth in ≤ 5 days. The 2-ka magma, however, interacted with a shallower silicic magma body and was heralded by several shallow intrusions during the preceding 50–60 days (Tepley et al. 2013), some of which possibly triggered small-volume phreatic/phreatomagmatic explosion(s) (Harpel et al. 2011; Cobeñas et al. 2012).

Monitoring

The Sacarosa TFD is the product of a voluminous explosive eruption of a dormant volcano, one initiated from a rapidly ascending magma that necessitates considering its monitoring ramifications. The paleosol beneath the Sacarosa TFD, lack of tephra deposits between it and the Anchi TFD, and both units' modeled ages indicate Misti was dormant for centuries to millennia before the Sacarosa eruption. Volcanoes reawakening from such slumber to produce VEI 5 or greater eruptions usually experience weeks to months of anticipatory unrest (e.g., Zen and Hadikusumo 1964; Endo et al. 1981; Jiménez et al. 1999).

The Sacarosa magma was staged at ~ 10 km depth, providing opportunities to detect unrest during emplacement and recharge of the parent magma, and upon its ascent from this level to erupt. Magma rising to erupt typically triggers earthquakes (McNutt and Roman 2015; White and McCausland 2016), deforms the crust (Poland and de Zeeuw-van Dalfsen 2021), and exsolves gas (Kern et al. 2022). While rare eruptions with very little precursory activity are known to occur (Roman and Cashman 2018), Misti's 2-ka eruption provides evidence that the volcano's next eruption would likely be preceded by several weeks or

months of forewarning (Harpel et al. 2011; Cobeñas et al. 2012; Tepley et al. 2013). Nonetheless, during both the 2-ka and possibly Sacarosa eruptions, the ultimate eruption-triggering intrusion ascended rapidly, implying that even with detectable precursory unrest, events can evolve quickly. The potential for a rapid-onset explosive eruption, even with precursory activity, highlights the value of a robust, multidisciplinary monitoring network. It additionally emphasizes that monitoring evidence for magma ascending within Misti's upper 10 km could be concerning, especially in consideration of the magma inferred to currently reside beneath the volcano (Moussallam et al. 2017; Vlastelic et al. 2022). Continuous engagement with stakeholders could further facilitate a rapid and appropriate response at the onset of unrest.

Hazards

The Sacarosa TFD represents a powerful VEI 5 eruption; while such an event is not the most likely eruption scenario, it provides a robust example of a paroxysmal event at Misti. Occasionally, VEI 4 events are considered paroxysmal eruptions for Misti, with the 2-ka eruption often used as an example of such an event (Sandri et al. 2014; Thouret et al. 2022). Nonetheless, the Sacarosa eruption demonstrates that VEI 5 events occur at Misti and confirms Mariño et al.'s (2016) assessment that such eruptions are possible. Late Pleistocene and Holocene TFDs, such as the Autopista and Pampa de los Huesos deposits, are analogous to the Sacarosa TFD and provide evidence of the volcano's continuing capacity to produce similarly powerful Plinian events. Mariño et al. (2007) mapped volcano hazards at Misti for eruptions up to VEI 6, with the zones for large-magnitude eruptions based on deposits from the volcano's 2-ka and Autopista eruptions and those from the 1600 CE Huaynaputina eruption. Nonetheless, both the 2-ka and Autopista eruptions are applied as examples of VEI 4 events, while the Cayma stage TFDs and subsequent PDC deposits are used as evidence for VEI 5 eruptions (Mariño et al. 2016). Using the Sacarosa TFD for comparison, we suggest that multiple VEI 5 events, including the Autopista eruption, have occurred after the Cayma stage. However, deposits at Misti with distributions and thicknesses sufficiently wider and larger than the Sacarosa TFD to suggest VEI 6 eruptions have yet to be recognized. If present, identification and characterization of deposits from VEI 6 eruptions at Misti could facilitate hazards mapping efforts.

Were a future eruption similar to the Sacarosa event to occur, it could cover Arequipa and the surrounding area with tens of centimeters of tephra (Fig. 1b), causing power failures, polluting water resources, and closing the airport (Blong 1984; Wilson et al. 2012; Thouret et al. 2022). While few fatalities generally occur as a direct result of tephra fall, respiratory irritation, and deaths from roof collapses and

other accidents are likely (Blong 1984; Horwell and Baxter 2006). Explosive eruptions also impact wide areas downwind, causing regional disruptions and destroying crops and pastures (e.g., Blong 1984; Jenkins et al. 2015; Elissondo et al. 2016). Fine, distal ash from such an eruption could additionally disrupt regional aviation hundreds to thousands of kilometers downwind (Guffanti et al. 2010; Jenkins et al. 2015; Prata and Rose 2015).

The R1 deposit (Fig. 2a; Legros 2001), while not coeval with the Sacarosa TFD, demonstrates that some of Misti's Cayma stage eruptions generated PDCs, as is common during VEI 5 eruptions (Newhall and Hoblitt 2002). Modeling results indicate that dense PDCs and dilute surges from Misti can flow 10 km or more from the vent and enter developed areas (Sandri et al. 2014; Charbonnier et al. 2020). Several of Arequipa's neighborhoods are also built upon and rapidly expanding farther into areas with PDC deposits from Misti's most recent Plinian eruption at 2 ka (Harpel et al. 2011; Cobeñas et al. 2012; Charbonnier et al. 2020), indicating that people are living within reach of these deadly phenomena. The 2-ka eruption was smaller in volume than the Sacarosa eruption, indicating that the PDC hazard would be exacerbated in the unlikely event of a future paroxysmal eruption like the Sacarosa event. Additionally, despite the arid environment and Misti's low available snow volume (Delaite et al. 2005; Harpel et al. 2011), lahars could be triggered in the volcano's drainages due to rain-induced remobilization of loose debris emplaced by such an eruption (Mazer et al. 2020; Thouret et al. 2022).

Conclusions

By characterizing the Sacarosa TFD and its eruption, we document the most voluminous VEI 5 eruption from Misti yet known and provide an example of one of the volcano's paroxysmal events. The Sacarosa TFD's 1.1–1.3 km³ (DRE) of magma had temperatures of 799–815 °C, fO_2 of NNO + 1.5, and trace-element concentrations typical for Misti. It remains unknown whether the Sacarosa eruption was preceded by antecedent unrest or intrusions into the edifice, but qualitative evidence suggests that the dacitic intrusion that eventually erupted rose rapidly from about 10 km to the surface. Upon the eruption's initiation, 3 km³ of tephra was emplaced over tens of hours and dispersed to the southwest by winds of ~10–20 m/s. The eruption deposited as much as 40 cm of tephra at 20 km downwind from the vent and voluminous fine ash was likely distributed much farther afield. The eruption maintained relatively steady conditions until about half of the deposit was emplaced and it either slightly increased in vigor or its degree of fragmentation decreased. The eruption reached a peak MER of 7.7×10^6 – 4.1×10^7 kg/s and column height

of 24–36 km asl. A similar future eruption, while unlikely, could distribute tens of centimeters of tephra over much of Arequipa, including its critical infrastructure. It could also be accompanied by PDCs and lahars.

The Sacarosa TFD was emplaced between 38.5 ka cal BP and 32.4 ka cal BP by the third eruption of the compositionally distinct Cayma stage. The Cayma stage eruptions began with deposition of the Cogollo TFD and PDC deposits, as early as 44.9 ka cal BP, and emplaced up to eight or more deposits over about 8.9–15.5 ky, including the newly named Anchi and Chuma TFDs (ESM 1). Several of Misti's Cayma stage and subsequent andesitic TFDs have distributions and thicknesses sufficiently comparable to the Sacarosa TFD, that they represent similarly voluminous and powerful eruptions. Voluminous, VEI 5 explosive eruptions appear more common at Misti than previously documented and likely are also more common in the CVZ than the scant published record suggests.

Supplementary Information The online version contains supplementary material available at <https://doi.org/10.1007/s00445-023-01654-z>.

Acknowledgements We are thankful for the assistance of Kevin Cueva, Nelida Manrique, David Valdivia, Marquinho Cabrera, Yhon Soncco, Saida Japura, Jessica Vela, Giancarlo Apaza, Gian Marco Escobar, Ashley How, Max Burnham, and Cecilia Harpel all of whom facilitated this project's completion. Discussions with Michael Dee, Jeff Pigati, Linda Scott Cummings, and R.A. Varney facilitated interpretation of new and published ¹⁴C ages. Insights into ¹⁴C age calibration and Bayesian modeling during this and earlier work from Christopher Bronk Ramsey, Erik Marsh, Andrew Millard, and Susan Lindauer are greatly appreciated. Detailed and thoughtful reviews by Jim Vallance and two anonymous reviewers helped improve this manuscript. Additional comments and suggestions by Larry Mastin and Chris Magirl and editorial input from Natalia Pardo and Andy Harris are also greatly appreciated. Any use of trade, firm, or product names is for descriptive purposes only and does not imply endorsement by the U.S. Government.

Funding Funding was provided by the U.S. Agency for International Development Bureau for Humanitarian Assistance (AID-OFDA-T-12-00001; Harpel), Fondo Nacional de Desarrollo Científico, Tecnológico y de Innovación Tecnológica del Consejo Nacional de Ciencia, Tecnología e Innovación Tecnológica del Perú (Convenio 158–2017-FONDECYT; Aguilar, Rivera), Universidad Nacional de San Agustín (UNSA Student Grant 151–2016; Cuno), and a 2019 Geological Society of America Lipman Graduate Student Research Grant (Takach).

Data availability All data is reported in the accompanying Online Resources with select data also reported in Harpel et al. (2023).

Code availability Code for Bayesian age model is available in the accompanying Electronic Supplementary Material 1.

Declarations

Conflict of interest The authors declare no competing interests.

Open Access This article is licensed under a Creative Commons Attribution 4.0 International License, which permits use, sharing, adaptation, distribution and reproduction in any medium or format, as long

as you give appropriate credit to the original author(s) and the source, provide a link to the Creative Commons licence, and indicate if changes were made. The images or other third party material in this article are included in the article's Creative Commons licence, unless indicated otherwise in a credit line to the material. If material is not included in the article's Creative Commons licence and your intended use is not permitted by statutory regulation or exceeds the permitted use, you will need to obtain permission directly from the copyright holder. To view a copy of this licence, visit <http://creativecommons.org/licenses/by/4.0/>.

References

- Adams NK, de Silva SL, Self S, Salas G, Schubring S, Permenter JL, Arbesman K (2001) The physical volcanology of the 1600 eruption of Huaynaputina, southern Peru. *Bull Volcanol* 62:493–518. <https://doi.org/10.1007/s004450000105>
- Aguiar R, Thouret J-C, Samaniego P, Wörner G, Jicha B, Paquette J-L, Suaña E, Finizola A (2022) Growth and evolution of long-lived, large volcanic clusters in the Central Andes: The Chachani Volcano Cluster, southern Peru. *J Volcanol Geoth Res* 426:107539. <https://doi.org/10.1016/j.jvolgeores.2022.107539>
- Ayala-Arenas JS, Cano NF, Rivera-Porras M, Gonzalez-Lorenzo CD, Watanabe S (2019) Dating volcanic ash and pumice stones from volcano El Misti, Peru, by thermoluminescence. *Quatern Int* 512:1–5. <https://doi.org/10.1016/j.quaint.2018.11.013>
- Bacon CR, Hirschmann MM (1988) Mg/Mn partitioning as a test for equilibrium between coexisting Fe-Ti oxides. *Am Mineral* 73:57–61
- Bernahola Portugal EF (2018) Tefroestratigrafía, alteraciones hidrotermales, geoquímica y evolución geológica del complejo volcánico Pichu – Pichu Arequipa - Perú. Bachelor Thesis, Universidad Nacional de San Agustín de Arequipa
- Biass S, Bonadonna C, Houghton BF (2019) A step-by-step evaluation of empirical methods to quantify eruption source parameters from tephra-fall deposits. *J Appl Volcanol* 8:1. <https://doi.org/10.1186/s13617-018-0081-1>
- Birnie RW, Hall JH (1974) The geochemistry of El Misti volcano, Peru fumaroles. *Bull Volcanol* 38:1–15. <https://doi.org/10.1007/BF02597797>
- Blong RJ (1984) Volcanic hazards: a sourcebook on the effects of eruptions. Academic Press, New York
- Bonadonna C, Costa A (2012) Estimating the volume of tephra deposits: a new simple strategy. *Geology* 40:415–418. <https://doi.org/10.1130/G32769.1>
- Bonadonna C, Costa A (2013) Plume height, volume, and classification of explosive volcanic eruptions based on the Weibull function. *Bull Volcanol* 75:742–761. <https://doi.org/10.1007/s00445-013-0742-1>
- Bonadonna C, Houghton BF (2005) Total grain-size distribution and volume of tephra-fall deposits. *Bull Volcanol* 67:441–456. <https://doi.org/10.1007/s00445-004-0386-2>
- Bonadonna C, Ernst GGJ, Sparks RSJ (1998) Thickness variations and volume estimates of tephra fall deposits: the importance of particle Reynolds number. *J Volcanol Geoth Res* 81:173–187. [https://doi.org/10.1016/S0377-0273\(98\)00007-9](https://doi.org/10.1016/S0377-0273(98)00007-9)
- Bonadonna C, Cioni R, Pistolesi M, Connor C, Scolla S, Pioli L, Rosi M (2013) Determination of the largest clast sizes of tephra deposits for the characterization of explosive eruptions: a study of the IAVCEI commission on tephra hazard modelling. *Bull Volcanol* 75:680. <https://doi.org/10.1016/j.jexplo.2009.05.003>
- Bronk Ramsey C (2009) Bayesian analysis of radiocarbon dates. *Radiocarbon* 51:337–360. <https://doi.org/10.1017/S0033822200033865>
- Bronk Ramsey C, Lee S (2013) Recent and planned developments of the program OxCal. *Radiocarbon* 55:720–730. <https://doi.org/10.1017/S0033822200057878>
- Cacya L, Mariño J, Rivera M, Thouret J-C (2007) La erupción pliniana “Autopista” del volcán Misti (21,000–11,000 años AP). *Bol Soc Geol Perú* 102:25–42
- Carey S, Sparks RSJ (1986) Quantitative models of the fallout and dispersal of tephra from volcanic eruption columns. *Bull Volcanol* 48:109–125. <https://doi.org/10.1007/BF01046546>
- Cas RAF, Wright JV (1987) Volcanic successions modern and ancient. Chapman & Hall, New York
- Charbonnier SJ, Thouret J-C, Guegneau V, Constantinescu R (2020) New insights into the 2070calyrBP pyroclastic currents at El Misti volcano (Peru) from field investigations, satellite imagery and probabilistic modeling. *Front Earth Sci*. <https://doi.org/10.3389/feart.2020.557788>
- Chávez Chávez JA (1992) La erupción del volcán Misti. Impresiones Zenit, Arequipa
- Cobeñas G, Thouret J-C, Bonadonna C, Boivin P (2012) The c.2030 yr BP Plinian eruption of El Misti volcano, Peru: eruption dynamics and hazard implications. *J Volcanol Geoth Res* 241–242:105–120. <https://doi.org/10.1016/j.jvolgeores.2012.06.006>
- Conrey RM, Bailey DG, Singer JW, Wagoner L, Parfitt B, Hay J, Keh O, Chang Z, Huang S (2023) Combined use of multiple external and internal standards in LA-ICP-MS analysis of bulk geological samples using lithium borate fused glass. *Geochem-Explor Env A* 23:geochem2023-001. <https://doi.org/10.1144/geochem2023-001>
- Cueva K (2016) Estudio geológico, petrográfico y geoquímico del volcán Sara Sara (Ayacucho). Ingeniero Thesis, Universidad Nacional de San Agustín de Arequipa
- Cuno JJ (2018) Estudio de la erupción del volcán Misti ocurrida hace 33,7 mil años AP, que emplazo el depósito “Sacarosa” en la ciudad de Arequipa. Ingeniero Thesis, Universidad Nacional de San Agustín de Arequipa
- Daggitt ML, Mather TA, Pyle DM, Page S (2014) AshCalc—a new tool for the comparison of the exponential, power-law, and Weibull models of tephra dispersion. *J Appl Volcanol* 3:7. <https://doi.org/10.1186/2191-5040-3-7>
- Delaite G, Thouret J-C, Sheridan M, Labazuy P, Stinton A, Souriot T, Van Westen C (2005) Assessment of volcanic hazards of El Misti and the city of Arequipa, Peru, based on GIS and simulations, with emphasis on lahars. *Z Geomorphol* 140:209–231
- de Silva SL, Alzueta J, Salas G (2000) The socioeconomic consequences of the A.D. 1600 eruption of Huaynaputina, southern Peru. In: McCoy FW, Heiken G (eds) Volcanic hazards and disasters in human antiquity. *Geol Soc Am Spec Pap* 345:15–24. <https://doi.org/10.1130/0-8137-2345-0.15>
- Elissondo M, Baumann V, Bonadonna C, Pistolesi M, Cioni R, Bertagnini A, Biass S, Herrero J-C, Gonzalez R (2016) Chronology and impact of the 2011 Cordón Caulle eruption, Chile. *Nat Hazards Earth Syst Sci* 16:675–704. <https://doi.org/10.5194/nhess-16-675-2016>
- Endo ET, Dzurisin D, Swanson DA (1990) Geophysical and observational constraints for shallow ascent rates of dacitic magma at Mount St. Helens. In: Ryan MP (ed) Magma Transport and Storage. Wiley, New York, pp 318–334
- Endo ET, Malone SD, Noson LL, Weaver CS (1981) Locations, magnitudes, and statistics of the March 20–May 18 earthquake sequence. In: Lipman PW, Mullineaux DR (eds) The 1980 eruptions of Mount St. Helens, Washington. U.S. Geol Surv Prof Pap 1250:93–107. <https://doi.org/10.3133/pp1250>
- Escobar GM (2021) Estudio de la erupción Pliniana del volcán Misti del Pleistoceno Superior que emplazo los depósitos del “Sandwich” en la ciudad de Arequipa. Ingeniero Thesis, Universidad Nacional Mayor de San Marcos

- Fei J, Zhang DD, Lee HF (2016) 1600 AD Huaynaputina eruption (Peru), abrupt cooling, and epidemics in China and Korea. *Adv Meteorol* 2016:3217038. <https://doi.org/10.1155/2016/3217038>
- Fernandez-Turiel JL, Perez-Torrado FJ, Rodríguez-Gonzalez A, Saavedra J, Carracedo JC, Rejas M, Lobo A, Osterrieth M, Carrizo JI, Esteban G, Gallardo J, Ratto N (2019) The large eruption 4.2 ka cal BP in Cerro Blanco, Central Volcanic Zone, Andes: Insights to the Holocene eruptive deposits in the southern Puna and adjacent regions. *Estud Geol* 75:e088. <https://doi.org/10.3989/egeol.43438.515>
- Fierstein J, Hildreth W (1992) The Plinian eruptions of 1912 at Novarupta, Katmai National Park, Alaska. *Bull Volcanol* 54:646–684. <https://doi.org/10.1007/BF00430778>
- Fierstein J, Nathenson M (1992) Another look at the calculation of fallout tephra volumes. *Bull Volcanol* 54:156–167. <https://doi.org/10.1007/BF00278005>
- Fontijn K, Ernst GGJ, Bonadonna C, Elburg MA, Mbede E, Jacobs P (2011) The ~4-ka Rungwe Pumice (South-Western Tanzania): a wind-still Plinian eruption. *Bull Volcanol* 73:1353–1368. <https://doi.org/10.1007/s00445-011-0486-8>
- Geschwind CH, Rutherford MJ (1995) Crystallization of microlites during magma ascent: the fluid mechanics of 1980–1986 eruptions at Mount St Helens. *Bull Volcanol* 57:356–370. <https://doi.org/10.1007/BF00301293>
- Ghiorso MS, Evans BW (2008) Thermodynamics of rhombohedral oxide solid solutions and a revision of the Fe-Ti two-oxide geothermometer and oxygen-barometer. *Amer J Sci* 308:957–1039. <https://doi.org/10.2475/09.2008.01>
- Gonnermann HM (2015) Magma fragmentation. *Annu Rev Earth Planet Sci* 43:431–458. <https://doi.org/10.1146/annurev-ev-earth-060614-105206>
- Grove TL, Kinzler RJ (1986) Petrogenesis of andesites. *Annu Rev Earth Planet Sci* 14:417–454. <https://doi.org/10.1146/annurev.ea.14.050186.002221>
- Guevara C (1968) Mapa geológica del cuadrángulo de Characato. *Servicio De Geología y Minería Del Perú* 1(100):000
- Guffanti M, Casadevall TJ, Budding K (2010) Encounters of aircraft with volcanic ash clouds: a compilation of known incidents, 1953–2009. *US Geological Survey Data Series* 545 ver. 1.0. <https://doi.org/10.3133/ds545>
- Hantke G, Parodi A (1966) Catalogue of the active volcanoes of the world including solfatara fields – Part XIX Colombia, Ecuador, and Peru. International Association of Volcanology, Rome
- Harpel CJ, Kushendratno, Stimac J, Avendaño Rodríguez de Harpel CF, Primulyana S (2019) The Orange Tuff: a late Pleistocene tephra-fall deposit emplaced by a VEI 5 silicic Plinian eruption in West Java, Indonesia *Bull Volcanol* 81:33. <https://doi.org/10.1007/s00445-019-1292-y>
- Harpel CJ, Cuno JJ, Takach MK, Rivera M, Aguilar R, Tepley FJ III, Garcia F (2023) Radiocarbon ages, whole-rock geochemical data, and pumice density measurements for the Sacarosa tephra-fall deposit, Misti volcano, southern Peru. *USGS Data Release*. <https://doi.org/10.5066/P9R5WD9B>
- Harpel CJ, Aguilar R, Rivera M, Tepley F, Takach M, Manrique N, Cuno JJ, Cueva K, Escobar GM, Allen I, Pawlak-Kjolhaug K, Sankovitch L, Topham J, Lewis C (2021) Tephrostratigraphy of Misti volcano, Arequipa, Peru from the late Pleistocene to the mid-15th century. Fall Meeting American Geophysical Union, New Orleans, 13–17 December, 2021AGUFM.V45C0145H
- Harpel CJ, de Silva S, Salas G (2011) The 2 ka eruption of Misti volcano, southern Peru—The most recent Plinian eruption of Arequipa's iconic volcano. *Geol Soc Am Spec Pap* 484. <https://doi.org/10.1130/2011.2484>
- Hildreth W, Drake RE (1992) Volcán Quizapu, Chilean Andes. *Bull Volcanol* 54:93–125. <https://doi.org/10.1007/BF00278002>
- Hogg AG, Heaton TJ, Hua Q, Palmer JG, Turney CSM, Southon J, Bayliss A, Blackwell PG, Boswijk G, Bronk Ramsey C, Petchey F, Reimer P, Reimer R, Wacker L (2020) SHCal13 Southern Hemisphere calibration, 0–50,000 years cal BP. *Radiocarbon* 62:759–778. <https://doi.org/10.1017/RDC.2020.59>
- Horwell CJ, Baxter PJ (2006) The respiratory health hazards of volcanic ash: a review for volcanic risk mitigation. *Bull Volcanol* 69:1–24. <https://doi.org/10.1007/s00445-006-0052-y>
- Houghton B, Carey RJ (2015) Pyroclastic fall deposits. In: Sigurdsson H, Houghton B, McNutt SR, Rymer H, Stix J (eds) *The encyclopedia of volcanoes*. Elsevier, Boston, pp 599–616. <https://doi.org/10.1016/B978-0-12-385938-9.00034-1>
- Houghton BF, Wilson CJN (1989) A vesicularity index for pyroclastic rocks. *Bull Volcanol* 51:451–462. <https://doi.org/10.1007/BF01078811>
- Instituto Nacional de Estadística e Informática (2018) Resultados definitivos de los Censos Nacionales 2017: XII de Población, VII de vivienda y III de Comunidades Indígenas —Arequipa. https://www.inei.gov.pe/media/MenuRecursivo/publicaciones_digitales/Est/Lib1551/
- Jenkins SF, Wilson T, Magill C, Miller V, Stewart C, Blong R, Marzocchi W, Boulton M, Bonadonna C, Costa A (2015) Volcanic ash fall hazard and risk. In: Loughlin SC, Sparks S, Brown SK, Jenkins SF, Vye-Brown C (eds) *Global volcanic hazards and risks*. Cambridge University Press, Cambridge, pp 173–222. <https://doi.org/10.1017/CBO9781316276273.005>
- Jiménez Z, Espíndola VH, Espíndola JM (1999) Evolution of the seismic activity from the 1982 eruption of El Chichon Volcano, Chiapas, Mexico. *Bull Volcanol* 61:411–422. <https://doi.org/10.1007/s004450050282>
- Johnson DM, Hooper PR, Conrey RM (1999) XRF analysis of rocks and minerals for major and trace elements on a single low dilution Li-tetraborate fused bead. *Adv X-Ray Anal* 41:843–867
- Jones TJ, McNamara K, Eychenne J, Rust AC, Cashman KV, Scheu B, Edwards R (2016) Primary and secondary fragmentation of crystal-bearing intermediate magma. *J Volcanol Geoth Res* 327:70–83. <https://doi.org/10.1016/j.jvolgeores.2016.06.022>
- Kennedy B, Spieler O, Scheu B, Kueppers U, Taddeucci J, Dingwell DB (2005) Conduit implosion during Vulcanian eruptions. *Geology* 33:581–584. <https://doi.org/10.1130/G21488.1>
- Kern C, Aiuppa A, de Moor JM (2022) A golden era for volcanic gas geochemistry? *Bull Volcanol* 84:43. <https://doi.org/10.1007/s00445-022-01556-6>
- Kiyosugi K, Connor C, Sparks RSJ, Crowther HS, Brown SK, Sierbert L, Wang T, Takarada S (2015) How many explosive eruptions are missing from the geologic record? Analysis of the Quaternary record of large magnitude explosive eruptions in Japan. *J Appl Volcanol* 4:17. <https://doi.org/10.1186/s13617-015-0035-9>
- Kueppers U, Scheu B, Spieler O, Dingwell DB (2006) Fragmentation efficiency of explosive volcanic eruptions: a study of experimentally generated pyroclasts. *J Volcanol Geoth Res* 153:125–135. <https://doi.org/10.1016/j.jvolgeores.2005.08.006>
- Le Bas MJ, Le Maitre RW, Streckeisen A, Zanettin B (1986) A chemical classification of volcanic rocks based on the Total Alkali-Silica diagram. *J Petrol* 27:745–750. <https://doi.org/10.1093/petrology/27.3.745>
- Leake BE, Woolley AR, Arps CES, Birch WD, Gilbert MC, Grice JD, Hawthorne FC, Kato A, Kisch HJ, Krivovichev VG, Linthout K, Laird J, Mandarino J, Maresch WV, Nickel EH, Schumacher JC, Smith DC, Stephenson NCN, Ungaretti L, Whittaker EJW, Youzhi G (1997) Nomenclature of Amphiboles: Report of the Subcommittee on Amphiboles of the International Mineralogical Association Commission on New Minerals and Mineral Names. *Can Mineral* 9:623–651. <https://doi.org/10.1180/minmag.1997.061.405.13>

- Legros F (1998) Tephrostratigraphie du volcan Misti (Perou) et modélisation des écoulements pyroclastiques. PhD Dissertation, Université Blaise Pascal
- Legros F (2001) Tephra stratigraphy of Misti volcano, Peru. *J South Am Earth Sci* 14:15–29. [https://doi.org/10.1016/S0895-9811\(00\)00062-6](https://doi.org/10.1016/S0895-9811(00)00062-6)
- Mamani M, Tassara A, Wörner G (2010) Composition and structural control of crustal domains in the central Andes. *Geochem Geophys Geosyst* 9:3. <https://doi.org/10.1029/2007GC001925>
- Mariño J, Rivera M, Cacya L, Thouret J-C, Macedo L, Salas G, Siebe C, Tilling R, Sheridan M, Chávez A, Zuñiga S (2007) Mapa de Peligros del Volcán Misti. <https://hdl.handle.net/20.500.12544/3612>
- Mariño J, Cueva K, Thouret J-C, Arias C, Finizola A, Antoine R, Delcher E, Cauchard C, Donnadiou F, Labazuy P, Japura S, Gusset R, Sanchez P, Ramos D, Macedo L, Lazarte I, Thouret L, Del Carpio J, Jaime L, Saintenoy T (2021) Multidisciplinary study of the impacts of the 1600 CE Huaynaputina eruption and a project for geosites and geo-touristic attractions. *Geoheritage* 13:64. <https://doi.org/10.1007/s12371-021-00577-5>
- Mariño J, Rivera M, Touret J-C, Macedo L (2016) Geología y mapa de peligros del volcán Misti. *INGEMMET Boletín Serie C: Geodinámica e Ingeniería Geológica* 60. <https://hdl.handle.net/20.500.12544/310>
- Marsh EJ, Bruno MC, Fritz SC, Baker P, Capriles JM, Hastorf CA (2018) IntCal, SHCal, or a mixed curve? Choosing a ^{14}C calibration curve for archaeological and paleoenvironmental records from tropical South America. *Radiocarbon* 60:925–940. <https://doi.org/10.1017/RDC.2018.16>
- Masías Nuñez del Prado P (1997) El Misti, biografía de un volcán. Club Italiano de Arequipa, Script S.A., Arequipa
- Mastin LG, Guffanti M, Servanckx R, Webley P, Barsotti S, Dean K, Durant A, Ewert JW, Neri A, Rose WI, Schneider D, Siebert L, Stunder B, Swanson G, Tupper A, Volentik A, Waythomas CF (2009) A multidisciplinary effort to assign realistic source parameters to models of volcanic ash-cloud transport and dispersion during eruptions. *J Volcanol Geoth Res* 186:10–21. <https://doi.org/10.1016/j.jvolgeores.2009.01.008>
- Mazer KE, Tomasek AA, Daneshvar F, Bowling LC, Frankenberger JR, McMillan SK, Novoa HM, Zeballos-Velarde C (2020) Integrated hydrologic and hydraulic analysis of torrential flood hazard in Arequipa, Peru. *J Contemp Water Res Educ* 171:93–110. <https://doi.org/10.1111/j.1936-704X.2020.3347.x>
- McNutt SR, Roman DC (2015) Volcanic seismicity. In: Sigurdsson H, Houghton B, McNutt SR, Rymer H, Stix J (eds) The encyclopedia of volcanoes. Elsevier, Boston, pp 1011–1034. <https://doi.org/10.1016/B978-0-12-385938-9.00059-6>
- Miwa T, Geshi N (2012) Decompression rate of magma at fragmentation: Inference from broken crystals in pumice of vulcanian eruption. *J Volcanol Geotherm Res* 227–228:76–84. <https://doi.org/10.1016/j.jvolgeores.2012.03.003>
- Moussallam Y, Peters N, Masias P, Apaza F, Barnie T, Schipper CI, Curtis A, Tamburello G, Aiuppa A, Philipson B, Giudice G, Pieri D, Davies AG, Oppenheimer C (2017) Magmatic gas percolation through the old lava dome of El Misti volcano. *Bull Volcanol* 79:46. <https://doi.org/10.1007/s00445-017-1129-5>
- Newhall CG, Hoblitt RP (2002) Constructing event trees for volcanic crises. *Bull Volcanol* 64:3–20. <https://doi.org/10.1007/s004450100173>
- Newhall CG, Self S (1982) The Volcanic Explosivity Index (VEI): an estimate of explosive magnitude for historical volcanism. *J Geophys Res* 87:1231–1238. <https://doi.org/10.1029/JC087iC02p01231>
- Ogburn DE (2012) Reconceiving the chronology of Inca imperial expansion. *Radiocarbon* 54:219–237. https://doi.org/10.2458/azu_js_rc.v54i2.16014
- Pearce JA, Peate DW (1995) Tectonic implications of the composition of volcanic arc magmas. *Annu Rev Earth Planet Sci* 23:251–285. <https://doi.org/10.1146/annurev.ea.23.050195.001343>
- Poland MP, de Zeeuw-van DE (2021) Volcano geodesy: a critical tool for assessing the state of volcanoes and their potential for hazardous eruptive activity. In: Papale P (ed) Hazards and disasters: forecasting and planning for volcanic hazards, risks, and disasters, vol 2. Elsevier, Amsterdam, pp 75–115. <https://doi.org/10.1016/B978-0-12-818082-2.00003-2>
- Prata F, Rose B (2015) Volcanic ash hazards to aviation. In: Sigurdsson H, Houghton B, McNutt SR, Rymer H, Stix J (eds) The encyclopedia of volcanoes, vol 2. Elsevier, Boston, pp 911–934. <https://doi.org/10.1016/B978-0-12-385938-9.00052-3>
- Putirka K (2016) Amphibole thermometers and barometers for igneous systems and some implications for eruption mechanisms of felsic magmas at arc volcanoes. *Amer Miner* 101:841–858. <https://doi.org/10.2138/am-2016-5506>
- Pyle D (1989) The thickness, volume, and grain size of tephra fall deposits. *Bull Volcanol* 51:1–15. <https://doi.org/10.1007/BF01086757>
- Reimer PJ, Austin WEN, Bard E, Bayliss A, Blackwell PG, Bronk Ramsey C, Butzin M, Cheng H, Edwards R, Friedrich M, Grootes PM, Guilderson TP, Hajdas I, Heaton TJ, Hogg AG, Hughen KA, Kromer B, Manning SW, Muscheler R, Palmer JG, Pearson C, van der Plicht J, Reimer RW, Richards DA, Scott EM, Southon JR, Turney CSM, Wacker L, Alphi F, Büntgen U, Capano M, Fahrni SM, Fogtmann-Schulz A, Friedrich R, Köhler P, Kudsk S, Miyake F, Olsen J, Reinig F, Sakamoto M, Sookdeo A, Talamo S (2020) The IntCal20 Northern Hemisphere radiocarbon age calibration curve (0–55 cal kBP). *Radiocarbon* 62:725–757. <https://doi.org/10.1017/RDC.2020.41>
- Rieder M, Cavazzini G, Yakonov YSD, Frank-Kamenetskii VA, Gottardi G, Guggenheim S, Koval PW, Moller G, Neiva AMR, Radoslovich EW, Robert JL, Sassi FP, Takeda H, Weiss ZK, Wones DR (1998) Nomenclature of the Micas. *Clays Clay Miner* 46:586–595. <https://doi.org/10.1346/CCMN.1998.0460513>
- Rivera M, Martin H, Le Pennec J-L, Thouret J-C, Gourgaud A, Gerbe M-C (2017) Petro-geochemical constraints on the source and evolution of magmas at El Misti volcano (Peru). *Lithos* 268–271:240–259. <https://doi.org/10.1016/j.lithos.2016.11.009>
- Rivera M, Samaniego P, Vela J, Le Pennec J-L, Guillou H, Paquette J-L, Liorzou C (2020b) The eruptive chronology of the Yuca-mane-Calientes compound volcano: a potentially active edifice of the Central Andes (southern Peru). *J Volcanol Geoth Res* 393:106787. <https://doi.org/10.1016/j.jvolgeores.2020.106787>
- Rivera M, Cueva K, Le Pennec J-L, Vela J, Samaniego P, Manrique N, Soncco Y (2020a) Geología y evaluación de peligros del volcán Sara Sara (Ayacucho). *INGEMMET Boletín Serie C: Geodinámica e Ingeniería Geológica* 78. <https://hdl.handle.net/20.500.12544/2992>
- Roman DC, Cashman KV (2018) Top-down precursory volcanic seismicity: implications for ‘stealth’ magma ascent and long-term eruption forecasting. *Front Earth Sci* 6:124. <https://doi.org/10.3389/feart.2018.00124>
- Rose WI (1972) Notes on the 1902 eruption of Santa María volcano, Guatemala. *Bull Volcanol* 36:29–45. <https://doi.org/10.1007/BF02596981>
- Rose WI (1993) Comment on another look at the calculation of fallout tephra volumes. *Bull Volcanol* 55:372–374. <https://doi.org/10.1007/BF00301148>
- Ruprecht P, Wörner G (2007) Variable regimes in magma systems documented in plagioclase zoning patterns: El Misti stratovolcano and Andahua monogenetic cones. *J Volcanol Geoth Res* 165:142–162. <https://doi.org/10.1016/j.jvolgeores.2007.06.002>
- Rutherford MJ, Hill PM (1993) Magma ascent rates from amphibole breakdown: An experimental study applied to the 1980–1986 Mt.

- St. Helens Eruptions. *J Geophys Res* 98:19667–19685. <https://doi.org/10.1029/93JB01613>
- Samaniego P, Rivera M, Manrique N, Schiavi F, Nauret F, Liorzou C, Ancellin M-A (2020) Linking magmatic processes and magma chemistry during the post-glacial to recent explosive eruptions of Ubinas volcano (southern Peru). *J Volcanol Geotherm Res* 407:107095. <https://doi.org/10.1016/j.jvolgeores.2020.107095>
- Sandri L, Thouret J, Constanesco R, Biass S, Tonini R (2014) Long-term multi-hazard assessment for El Misti volcano (Peru). *Bull Volcanol* 76:771. <https://doi.org/10.1007/s00445-013-0771-9>
- Sarna-Wojcicki AM, Shipley S, Waitt RB, Dzurisin D, Wood SH (1981) Areal distribution, thickness, mass, volume, and grain size of air-fall ash from the six major eruptions of 1980. In: Lipman PW, Mullineaux DR (eds) *The 1980 eruptions of Mount St. Helens*, vol 1250. USGS Prof Paper, Washington, pp 577–600
- Scandone R, Malone SD (1985) Magma supply, magma discharge and readjustment of the feeding systems of Mount St. Helens during 1980. *J Volcanol Geotherm Res* 23:239–262. [https://doi.org/10.1016/0377-0273\(85\)90036-8](https://doi.org/10.1016/0377-0273(85)90036-8)
- Scasso R, Corbella H, Tiberi P (1994) Sedimentological analysis of the tephra from 12–15 August 1991 eruption of Hudson volcano. *Bull Volcanol* 56:121–132. <https://doi.org/10.1007/BF00304107>
- Siebert L, Simkin T, Kimberley P (2010) *Volcanoes of the world*. University of California Press, Berkeley
- Socha DM, Reinhard J, Chávez J, Perea R (2021) Inca human sacrifices on Misti volcano (Peru). *Lat Am Antiq* 32:138–153. <https://doi.org/10.1017/laq.2020.78>
- Sparks RSJ (1986) The dimensions and dynamics of volcanic eruption columns. *Bull Volcanol* 48:3–15. <https://doi.org/10.1007/BF01073509>
- Sparks RSJ, Bursik MI, Carey SN, Gilbert JS, Glaze JS, Sigurdsson H, Woods AW (1997) *Volcanic plumes*. John Wiley & Sons, New York
- Spieler O, Kennedy B, Kueppers U, Dingwell DB, Scheu B, Taddeucci J (2004) The fragmentation threshold of pyroclastic rocks. *Earth Planet Sc Lett* 226:139–148. <https://doi.org/10.1016/j.epsl.2004.07.016>
- Sulpizio R (2005) Three empirical methods for the calculation of distal volume of tephra-fall deposits. *J Volcanol Geoth Res* 145:315–316. <https://doi.org/10.1016/j.jvolgeores.2005.03.001>
- Sun S-S, McDonough WF (1989) Chemical and isotopic systematics of oceanic basalts: implications for mantle composition and processes. In: Saunders AD, Norry MJ (eds.) *Magmatism in ocean basins* *Geol Soc Spec Publ* 42:313–345. <https://doi.org/10.1144/GSL.SP.1989.042.01.19>
- Takach MK, Tepley FJ, Harpel CJ, Aguilar R, Rivera M (2021) Deciphering the petrology of a hazardous volcano: magma storage conditions, remobilization, and timescales inferred from tephra-fall deposits from Misti volcano, Peru. *Geological Society of America Abstracts with Programs* 53(6):2021. <https://doi.org/10.1130/abs/2021AM-368132>
- Takach MK, Tepley FJ, Harpel CJ, Aguilar R, Rivera M (in review) To mix or not to mix: details of magma storage, recharge, and remobilization during the Pacheco stage at Misti volcano, Peru (≤ 21 –2 ka). *J Petrol*
- Tepley FJ III, de Silva S, Salas G (2013) Magma dynamics and petrological evolution leading to the VEI 5 2000 BP eruption of El Misti volcano, southern Peru. *J Petrol* 54:2033–2065. <https://doi.org/10.1093/petrology/egt040>
- Thouret J-C, Suni J, Eissen J-P (1999) Assessment of volcanic hazards in the area of Arequipa City, based on the eruptive history of the Misti volcano, southern Peru. *Z Geomorph NF S-B* 114:89–112
- Thouret J-C, Finizola A, Fornari M, Legeley-Padovani A, Suni J, Frechen M (2001) Geology of El Misti volcano near the city of Arequipa, Peru. *Geol Soc Am Bull* 113:1593–1610. [https://doi.org/10.1130/0016-7606\(2001\)113%3c1593:GOEMVN%3e2.0.CO;2](https://doi.org/10.1130/0016-7606(2001)113%3c1593:GOEMVN%3e2.0.CO;2)
- Thouret J-C, Arapa E, Charbonnier S, Guerrero A, Kelfoun K, Cordoba G, Rodriguez D, Santoni O (2022) Modeling tephra fall and sediment-water flows to assess their impacts on a vulnerable building stock in the city of Arequipa, Peru. *Front Earth Sci* 10:865989. <https://doi.org/10.3389/feart.2022.865989>
- Thouret J-C, Legros F, Gourgard A, Macedo M-L (1996) El Misti stratovolcano south Peru: eruptive history and implications for hazard assessment. *Andean Geodynamics, Extended Abstracts of the Third International Symposium on Andean Geodynamics*, St. Malo, 17–19 September, pp 251–254. <https://www.documentat.ion.ird.fr/hor/fdi:010008571>
- Topham J, Tepley FJ III, Takach MK, Harpel CJ, Rivera M, Aguilar R, Cuno JJ (2021) Understanding the petrology and geochemistry of biotite-bearing dacitic/rhyolitic tephra-fall deposits from Misti volcano, Peru. *Geological Society of America Abstracts with Programs* 53(6):2021. <https://doi.org/10.1130/abs/2021AM-368353>
- Trumbore SE (2000) Radiocarbon geochronology. In: Noller JS, Sowers JM, Lettis WR (eds) *Quaternary geochronology methods and applications*. American Geophysical Union, Washington, D.C., pp 41–60. <https://doi.org/10.1029/RF004p0041>
- Vlastelic I, Apaza F, Masias P, Rivera M, Pior J-L, Gannoun A (2022) Probing the hidden magmatic evolution of El Misti volcano (Peru) with Pb isotope composition of fumaroles. *Bull Volcanol* 84:17. <https://doi.org/10.1007/s00445-021-01521-9>
- Walker GPL (1973) Explosive volcanic eruptions – a new classification scheme. *Geol Rundsch* 62:431–446. <https://doi.org/10.1007/BF01840108>
- Walker GPL (1980) The Taupo Pumice: product of the most powerful known (ultraplinian) eruption? *J Volcanol Geoth Res* 8:69–94. [https://doi.org/10.1016/0377-0273\(80\)90008-6](https://doi.org/10.1016/0377-0273(80)90008-6)
- Walker GPL (1981) Plinian eruptions and their products. *Bull Volcanol* 44:223–240. <https://doi.org/10.1007/BF02600561>
- White R, McCausland W (2016) Volcano-tectonic earthquakes: a new tool for estimating intrusive volumes and forecasting eruptions. *J Volcanol Geoth Res* 309:139–155. <https://doi.org/10.1016/j.jvolgeores.2015.10.020>
- Williams SN, Self S (1983) The October 1902 Plinian eruption of Santa Maria volcano, Guatemala. *J Volcanol Geoth Res* 16:33–56. [https://doi.org/10.1016/0377-0273\(83\)90083-5](https://doi.org/10.1016/0377-0273(83)90083-5)
- Wilson M (1989) *Igneous petrogenesis, a global tectonic approach*. Springer, New York
- Wilson TM, Stewart C, Sword-Daniels V, Leonard GS, Johnston DM, Cole JW, Wardman J, Wilson G, Barnard ST (2012) Volcanic ash impacts on critical infrastructure. *Phys Chem Earth* 45–46:5–23. <https://doi.org/10.1016/j.pce.2011.06.006>
- Wright H, Rivera M, Vela Valdez J, Harpel C (2018) Tefrostratigrafía post-glacial del Volcán Ubinas, Perú. In: Aguilar R (ed) *Libro de Resúmenes: VIII Foro Internacional los Volcanes y su Impacto*, Arequipa, Peru, 26–27 April
- Zen MT, Hadikusumo D (1964) Preliminary report on the 1963 eruption of Mt. Agung in Bali (Indonesia). *Bull Volcanol* 27:269–299. <https://doi.org/10.1007/BF02597526>